AD-A070 896 EMTEC ENGINEERING INC BERKELEY CA F/G 19/1
SCATTERING BY BURIED FINITE CYLINDRICAL DIELECTRIC LAND MINES.(U)
MAR 79 S CHANG DAAK70-78-C-0168
UNCLASSIFIED NL

1 OF 1
AD A070896

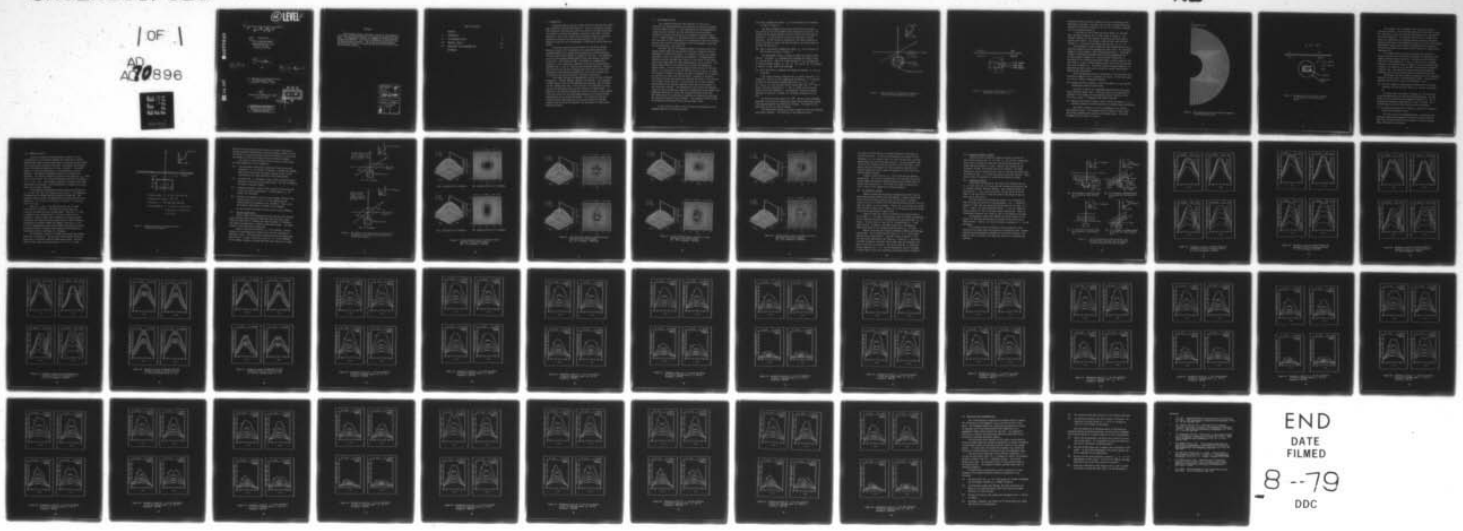

END
DATE FILMED
8-79
DDC

(12) LEVEL II

(6) SCATTERING BY BURIED FINITE CYLINDRICAL DIELECTRIC LAND MINES,

(10) Prepared by

Shu-Kong Chang, ~~Ph.D.~~

FMtec Engineering, Inc.
P.O. Box 679
Berkeley, CA 94701

(9) Final Report,

(12) 52 P.

for

(11) 20 Mar 79

U.S. Army Mobility Equipment Research
and Development Command
Fort Belvoir, Virginia 22060

(15) Contract No. DAAK70-78-C-0168

March 20, 1979

ABSTRACT

The unimoment method is applied to solve the electromagnetic scattering by a buried dielectric finite cylinder simulating a land mine. The computational results are reported at 700 MHz, 800 MHz, 900 MHz, and 1000 MHz. The fields are presented in graphical form including parametric studies. The results will greatly enhance the ability of engineers in designing and improving effective land mine detection systems.

TABLE OF CONTENTS

I. INTRODUCTION

Land mines made of plastic or other dielectric material has caused many casualties during recent conflicts. They are continuously causing more casualties even many years after the conflicts, because these mines are difficult to detect and complete clearing of such mines is almost impossible. One of the reasons that an effective detection system for dielectric land mines has not yet been developed is the lack of theoretical data for the electromagnetic scattering by buried dielectric bodies.

In order to generate the data usable for the design of mine detection systems, this investigation has successfully applied the unimoment method [1] to compute the scattering by a buried dielectric finite cylinder which simulates a dielectric land mine. The computation uses the Finite Element Method (FEM) to treat the boundary conditions of the mine. The solution of FEM is terminated at a mathematical sphere by a set of analytical expansions which satisfy the continuity conditions of E and H fields on the air-ground interface. Owing to the versatility of the FEM in matching the mine surface and the fast convergence of the analytical expansions, we are able to compute the scattering by the buried dielectric land mines efficiently.

This report provides the computational results for four different frequencies: 700 MHz, 800 MHz, 900 MHz, and 1000 MHz. Five different incident angles, each with two different polarizations, are considered for the incident plane wave. Total electric field amplitude is calculated on the horizontal planes at five different altitude levels. In addition to the selected 3-dimensional and contour plots of the electric field, the results are also presented parametrically to show the best understanding of the scattering problem. It is believed that this study and future investigations on more exact models will provide valuable data assisting the engineers for the design of reliable mine detection systems.

II. THE UNIMOMENT METHOD

The unimoment method was first published in 1972 [1] to generalize the moment method for the radiation and scattering problems involving material bodies. It was then applied to the inhomogeneously loaded biconical antennas [2], the scattering by two dimensional dielectric cylinders [3], and by axially symmetric dielectric bodies [4, 5]. Recent discovery of the generalization of Sommerfeld integrals and a new type of field expansions in two medium half spaces [6] had made possible the extension of the method to the electromagnetic scattering by buried dielectric land mines [7].

The basic idea of the unimoment method is to combine the Finite Element Method (FEM) with the analytic solutions so that the maximum advantages are obtained from both. The analytic solutions are usually expressed in terms of truncated series expansions. Although analytic expansions usually represent the fields of a vast region in the space, they are only applicable to simply shaped objects such as spheres. The FEM has been noted for its flexibility of fitting the boundary of general shapes. For the scattering problems which involve an infinite space, it is impractical to use the FEM for the entire space. In order to minimize the number of unknowns, the FEM is terminated at two spheres, one encloses the entire mine and the other is imbedded in the mine. The spherical vector wave expansions represent the fields in the interior of the sphere inside the mine. In the exterior of the outer sphere, complications of the analytic expansions occur due to the presence of the air-ground interface. The computation in this report has employed a special type of vector wave expansions incorporated with the generalized Sommerfeld integrals to satisfy the air-ground boundary conditions. The coefficients of the analytical expansions are obtained by enforcing the continuity conditions on the spheres. The scattered fields can then be calculated from the coefficients and the modal fields.

In this section we shall briefly describe the procedures of the unimoment method in the following steps:

(1) Draw a mathematical sphere S_1 to enclose the entire land mine as shown in Figure 1.

The sphere mathematically divides the space into two parts. The interior of the sphere (Region III) contains the land mine. The exterior of the sphere (Regions I and II) involves the lossy ground and the air. The selection of the size for the sphere is quite arbitrary. For efficiency and convenience, the sphere should be as small as possible to reduce the FEM calculation, and large enough to enclose the entire mine.

(2) Draw a supplemental mathematical sphere S_2 in the interior of the land mine as shown in Figure 2.

The supplemental sphere is drawn to reduce the region of FEM further. The sphere S_2 mathematically separates the region inside S_1 into two parts. Region IV is the interior of S_2 and Region III is the area between spheres S_1 and S_2. The size of S_2 is arbitrary as long as it stays within the mine body.

(3) Solve the Maxwell's equations for Region III between S_1 and S_2 using FEM.

The original Maxwell's equation has six vector components in 3-dimensions. Because of axial symmetry of the geometry, it is possible to reduce the two coupled azimuthal potentials $\psi_1 = k_o \rho E_\phi$ and $\psi_2 = k_o \rho H_\phi$ for each azimuthal Fourier series mode with $e^{jm\phi}$ variations. All other components of E and H fields can be directly obtained from these potentials. The potentials satisfy two coupled differential equations in Region III including the boundary of the mine.

By using the Fourier series of $e^{jm\phi}$ and the coupled azimuthal potentials we are able to reduce the original three dimensional problem into many much smaller two dimensional problems. The amount of computer time can thus be greatly reduced.

The differential equations are then changed to their corresponding variational integrals. The functions of the potentials which

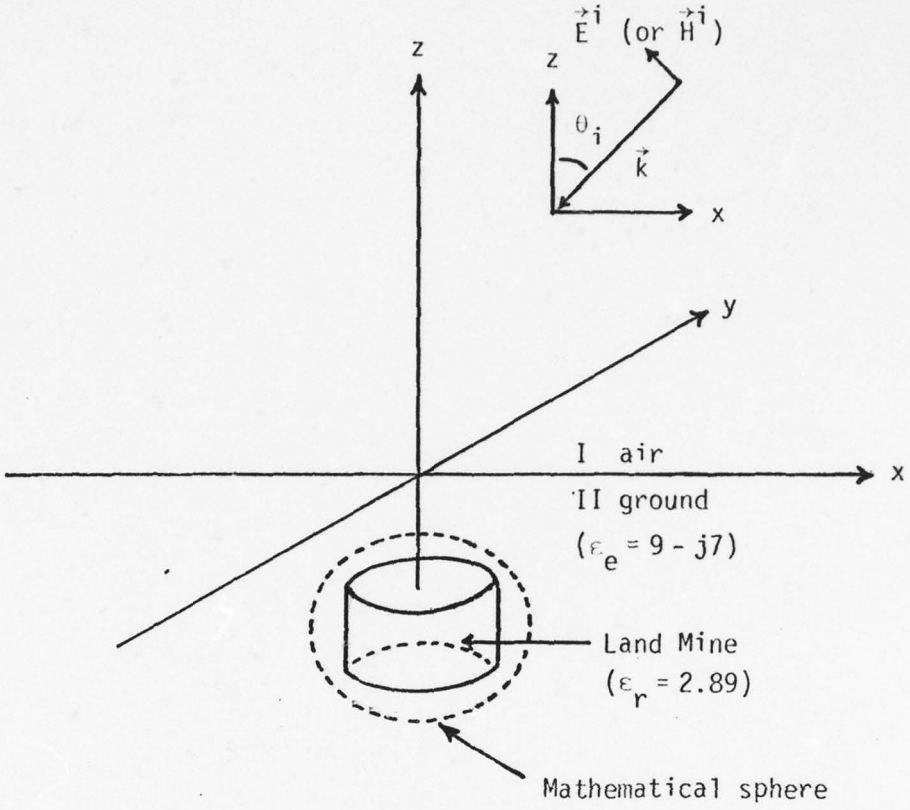

Figure 1. The illustration of the buried dielectric land mine and the mathematical sphere

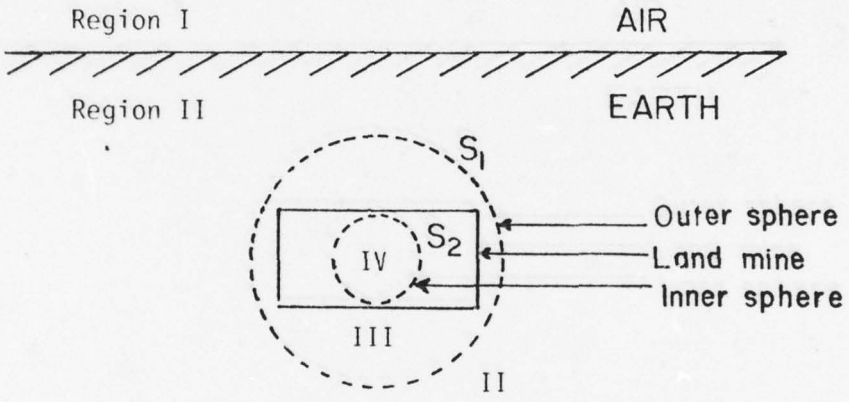

Figure 2. Minimization of FEM region III by a supplemental inner sphere S_2

stationarize the variational integral are also the solutions of the differential equations. The basic idea of FEM is to approximate the potentials by piecewise polynomials so that the variational integrals can be evaluated analytically.

In the FEM, we first divide the entire Region III into many small triangular elements such as those shown in Figure 3. The triangles conform with the surfaces of the mine, the inner sphere, and the outer sphere. The elements inside the mine have dielectric constant $\varepsilon_r = 2.89$ and those outside the mine have $\varepsilon_e = 9 - j7$.

The potentials in each triangle are then represented by interpolating polynomials passing through each nodal value. The variational integral in each element is then evaluated analytically. The global integral is obtained by summing up the element integrations over all the elements in Region III. The variational formulation is stationary if its differentiation with respect to nodal values is zero. This leads to a set of linear equations which can be used to solve for the fields in Region III. The matrix involved in these equations is a banded sparse matrix which can be solved by a special sparse matrix algorithm very efficiently.

Since the boundary values on the spheres are not specified, the solutions of Region III are in general not unique. In fact they result in a set of linearly independent solutions.

(4) Expand the field in Region IV inside the sphere S_2 by using the conventional spherical vector waves.

The field in Region IV is expanded analytically by the conventional spherical vector waves. Since the origin of the coordinate is included in this region, only the spherical Bessel functions of the first kind $j_n(kr)$ is required as the radial functions.

(5) Represent the field in Region I and II outside the sphere S_1 by multipole expansions which satisfy the air-ground boundary conditions.

The fields in Regions I and II are decomposed into incident and scattered fields. The scattered fields in Region II (the earth) are further decomposed into primary and secondary waves. The field decompositions are shown in Figure 4.

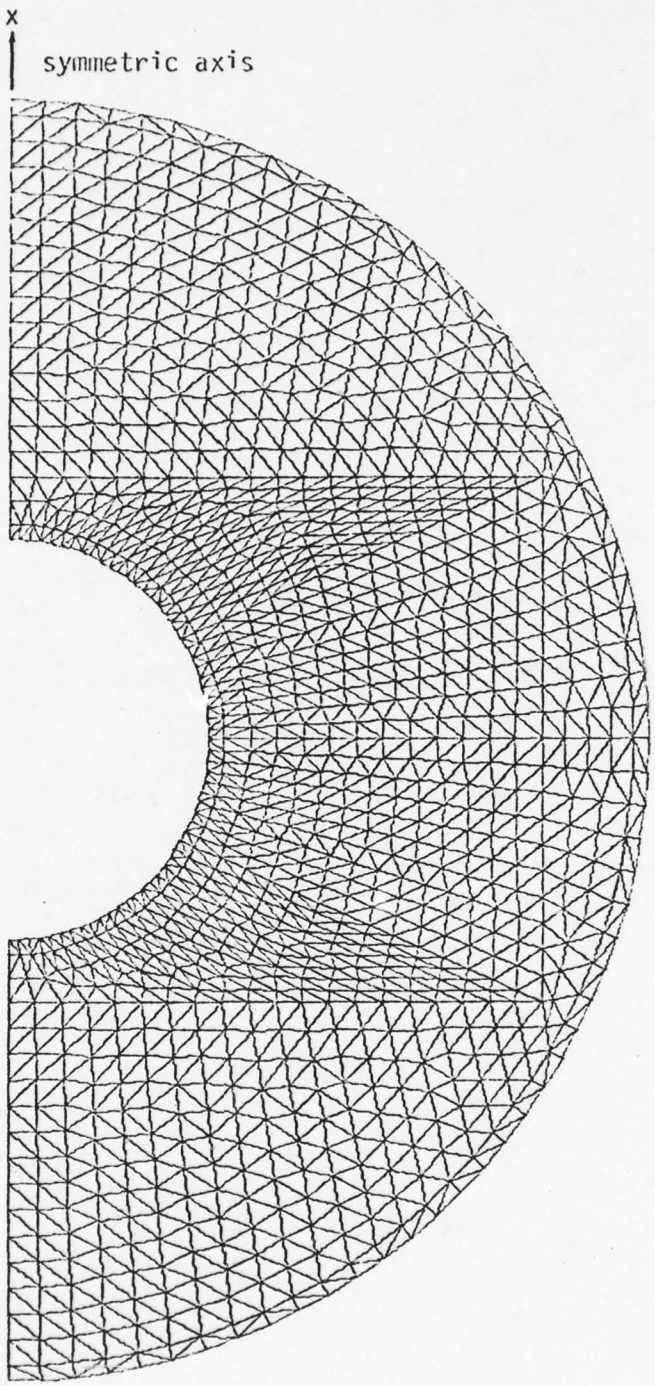

Figure 3. The construction of the triangular elements in the meridianal plane

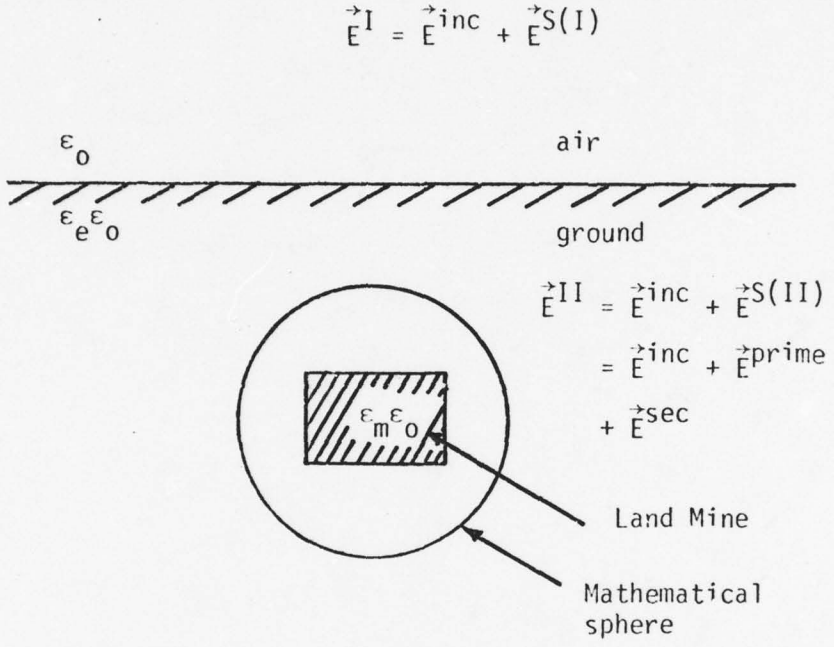

Figure 4. Decomposition of analytical solutions in the exterior of the mathematical sphere

The primary field is expanded into a specially designed multipole expansion. The rectilinear spherical vector waves in which the rectangular vectors and the spherical harmonics are combined for the vector potentials. This type of combination was introduced to reduce the complexities in enforcing both the spherical and planar boundary conditions on the mathematical sphere and on the earth surface. Supplemental terms using horizontal rotating multipoles have been discovered and added to the primary field expansions to speed up the convergence [6].

The primary fields are then transformed into cylindrical harmonics by using the Fourier-Bessel integrals of transforming the spherical-Hankel-Legendre functions. By enforcing the continuity conditions of the tangential E and H fields on the air-ground interface, the secondary fields in Region II and the scattered field in Region I are found to be in the form of "Generalized Sommerfeld integrals" [6]. The expansions with the generalized Sommerfeld integrals satisfy the air-ground boundary condition term-by-term.

The analysis has thus yielded a converging multipole expansion technique for the fields in two-medium half spaces. The same set of expansion coefficients are used in both Regions I and II.

(6) Solve the expansion coefficients by enforcing the continuity conditions on both the outer sphere S_1 and the inner sphere S_2.

The three sets of solutions in Regions II, III, and IV are solved individually by the previously described methods. We then couple all the solutions on the mathematical spheres S_1 and S_2 by using the continuity conditions of E and H fields. The incident waves are the driving fields for the calculations.

(7) Calculate scattered fields in Region I (the air) by using the coefficients and modal fields.

The final step of the unimoment method is to generate the required scattered electromagnetic fields by a buried land mine. The fields on planes parallel to the ground at different heights above the ground are calculated.

III. NUMERICAL RESULTS

Using the unimoment method described in Section II, this investigation has successfully computed the scattering of electromagnetic waves from a buried object which is electrically very similar to an antipersonnel dielectric land mine. The geometrical configuration of the proposed computation is shown in Figure 5. The buried target is a finite cylinder which is 5.5 cm high and 11.2 cm in diameter. The dimensions approximate those of an antipersonnel land mine. The relative dielectric constant of the target is $\varepsilon_r = 2.89$, which is that of TNT. The relative dielectric constant of the ground is $\varepsilon_e = 9.0 - j7.0$. The top edge of the mine is buried 5.5 cm under the surface of the ground. This configuration is believed to be very close to the actual situation.

The scattering configuration involves plane wave incidence at $\theta_i = 0°$, 30°, 45°, 60°, 75° reference to the z-axis. The frequencies considered are at 700 MHz, 800 MHz, 900 MHz, and 1000 MHz. The scattered electric fields are computed on the planes parallel to the ground at z = 0" (0 cm), 1" (2.5 cm), 2" (5.08 cm), 3" (7.62 cm), and 5" (12.7 cm).

The axes x and y are defined so that the x-z plane is the plane of incidence. Two different kinds of polarizations are considered for each incident angle. They are $\vec{E}$ in the x-z plane (or H-Y incidence) and $\vec{H}$ in the x-z plane (or E-Y incidence). Owing to their basic differences in refraction and scattering, the two polarizations should result in quite different scattered field patterns except the symmetric case when $\theta_i = 0°$. In all the computations shown in this report, the original incident plane waves (before reflection and refraction of the ground) are considered to have an amplitude of 1 volt/meter.

The computation involves 5 incident angles each with 2 polarizations at 4 frequencies. For each case, the scattered fields are generated at 5 different parallel planes above ground. The total number of data cases to be presented are $5 \times 2 \times 4 \times 5 = 200$.

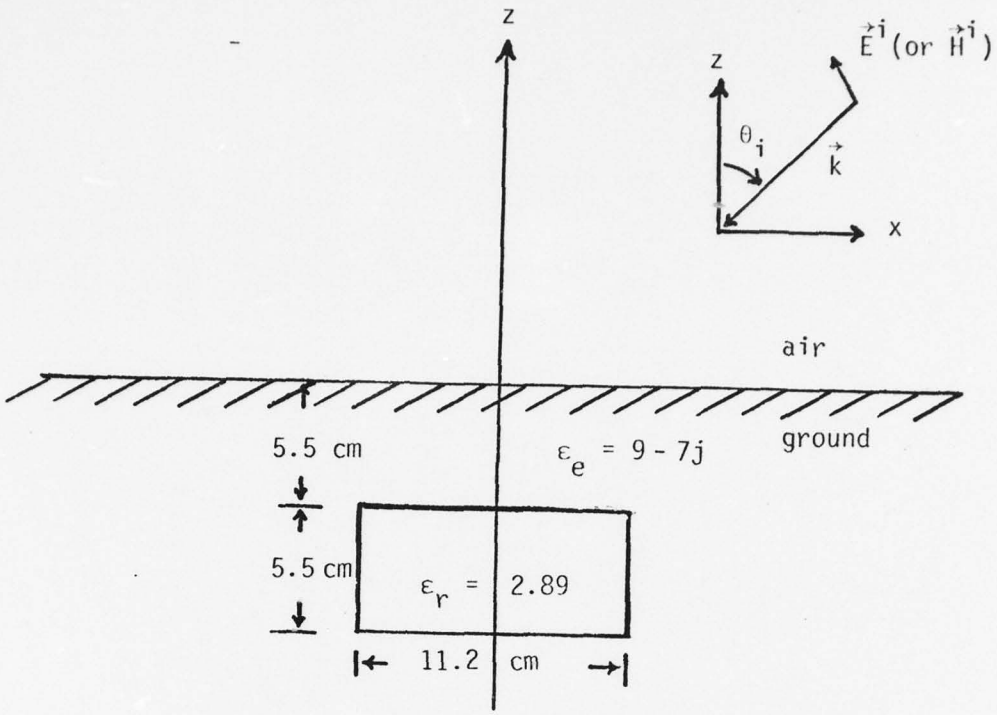

Incident angles θ_i = 0°, 30°, 45°, 60°, 75°

Incident polarizations = $\vec{E}^i$ or $\vec{H}^i$

Frequencies f = 700, 800, 900, 1000 MHz

Field computed at z = 0" (0 cm), 1" (2.54 cm),
2" (5.08 cm), 3" (7.62 cm),
5" (12.7 cm)

Figure 5. Proposed scattering configurations and computational parameters

Because of the vast amount of data involved, we have specifically designed graphical presentations involving parametric studies so that the result can be well understood and will be beneficial in assisting the engineers to design and improve the mine detection systems.

The results of the scattered E-fields obtained in this report are shown graphically in four categories.

(1) 3-D and contour plots of the scattered E-field on the earth surface for θ_i = 0° and 45° at frequency = 700 MHz and 1000 MHz. These few selected plots will show a general picture of the field pattern on a plane parallel to the ground surface.

(2) Incident angle θ_i parametric curves of the scattered E-field along the x and y axis on the ground plane. All four frequencies are shown in separate figures.

(3) Frequency parametric curves of the scattered E-field along the x and y axis on the ground plane. Incident angles θ_i = 0° and 45° are considered.

(4) Altitude (z) parametric curves of the scattered E-field on the lines parallel to x or y axis. All the combinations of incident angles and frequencies are considered. That is, all the proposed computations are shown in this category.

We shall discuss the details of the results in the following:

(1) 3-D and contour plots

Figure 6 shows the configuration of the land mine, the incident waves, and the square surface of which the fields are to be shown. Figure 6a shows the H-Y incidence and Figure 6b shows E-Y incidence. The fields are presented in a square on the earth surface. The square extends to twice the radius of the mine.

Figure 7 shows the E-field for θ_i = 0° at 700 MHz. Perfect symmetry is found between the results of H-Y and E-Y incidences by switching x and y. The distributions flatten out near the center area above the mine. Figure 8 shows the result for θ_i = 0° at 1000 MHz. At this higher frequency, the peak amplitude drops about 10 ~ 15 mV/M

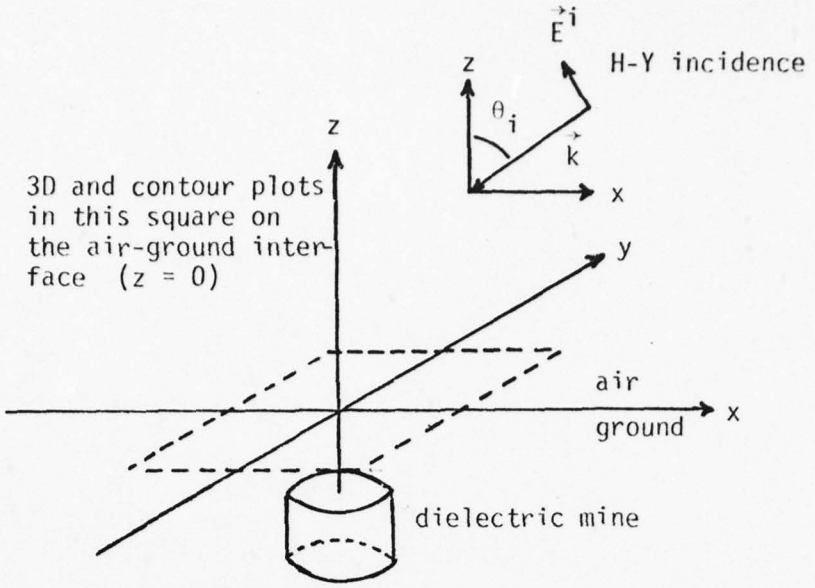

(a) H-Y incidence

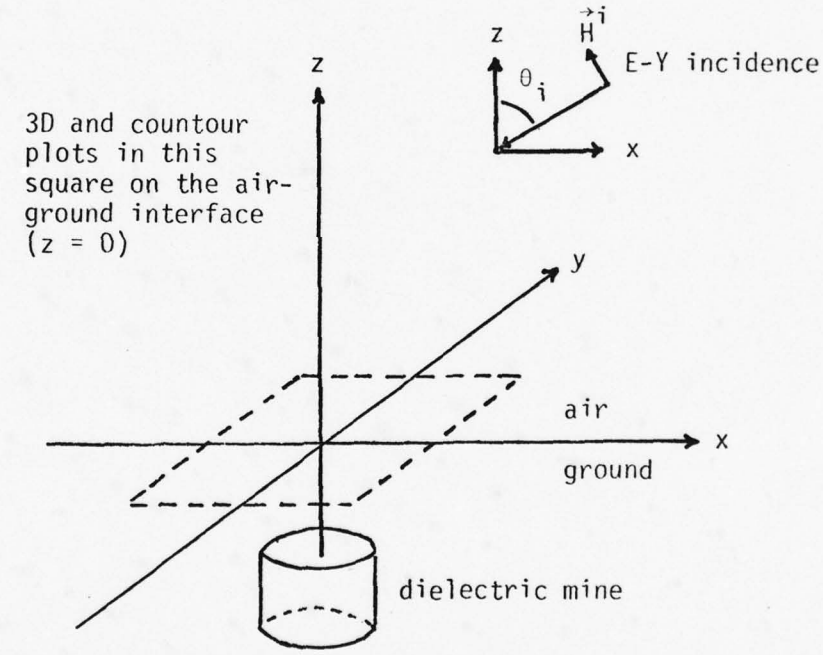

(b) E-Y incidence

Figure 6. The square on the ground plane in which the 3D and contour plots of the scattered electric fields will be shown

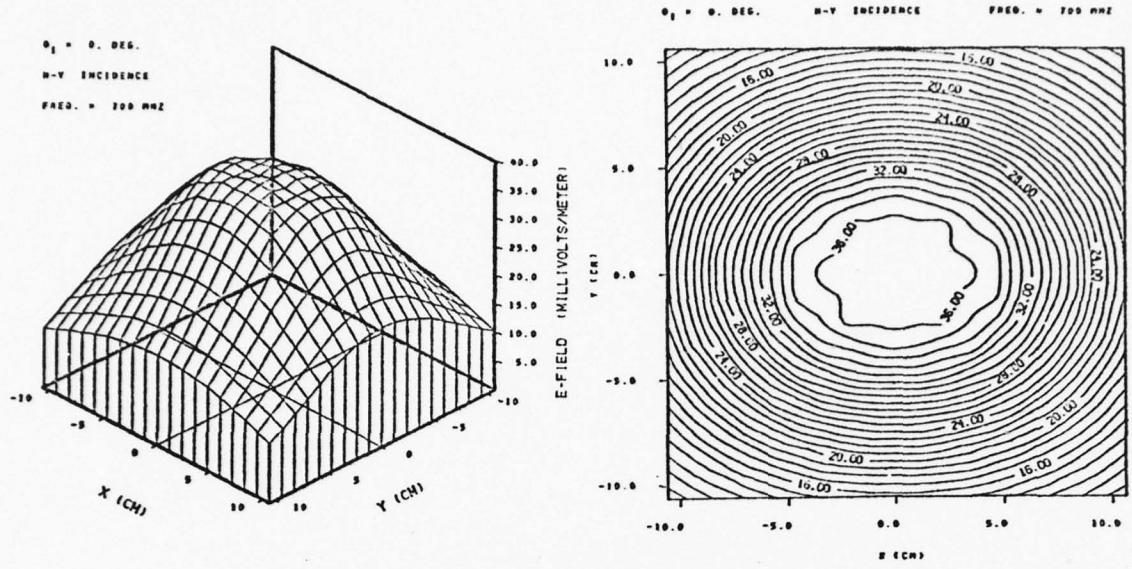

(a) 3-D plot for H-Y incidence (b) Contour plot for H-Y incidence

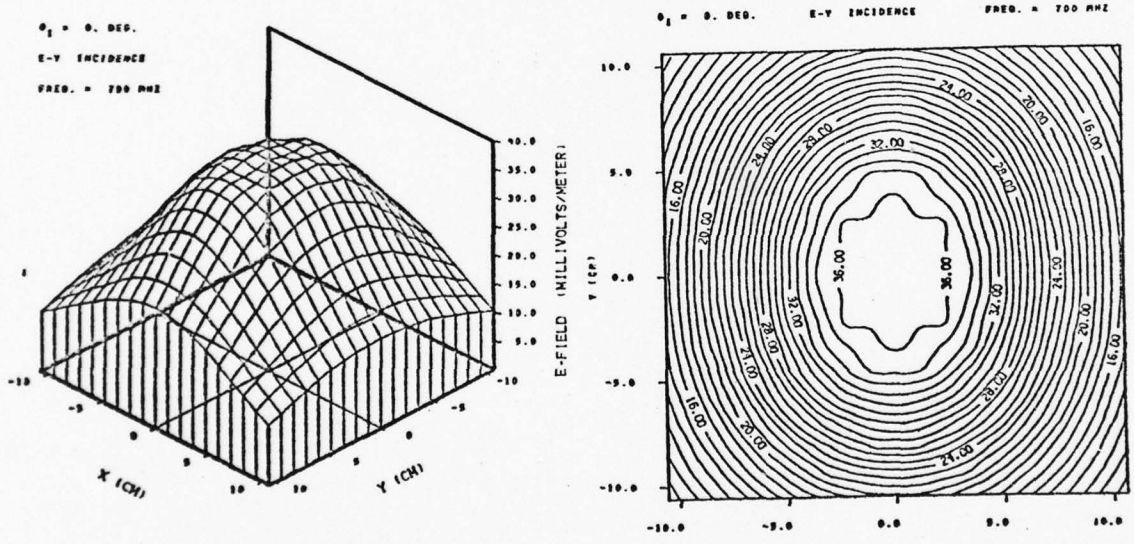

(a) 3-D plot for E-Y incidence (b) Contour plot for E-Y incidence

Figure 7. 3-D and contour plots of scattered E-field amplitude on the earth surface (θ_i = 0°, frequency = 700 MHz)

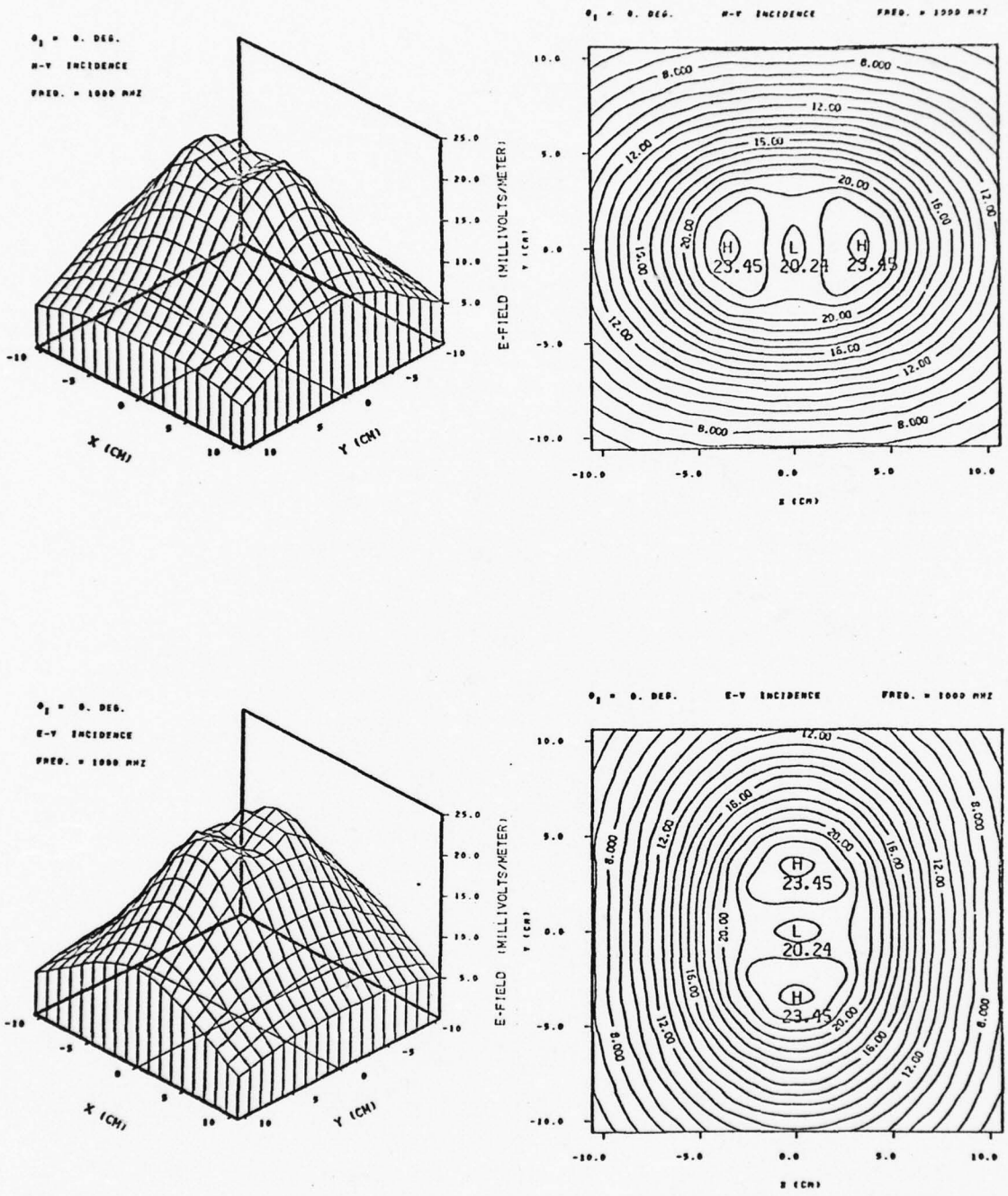

Figure 8. 3-D and contour plots of scattered E-field amplitude on the earth surface (θ_i = 0°, frequency = 1000 MHz)

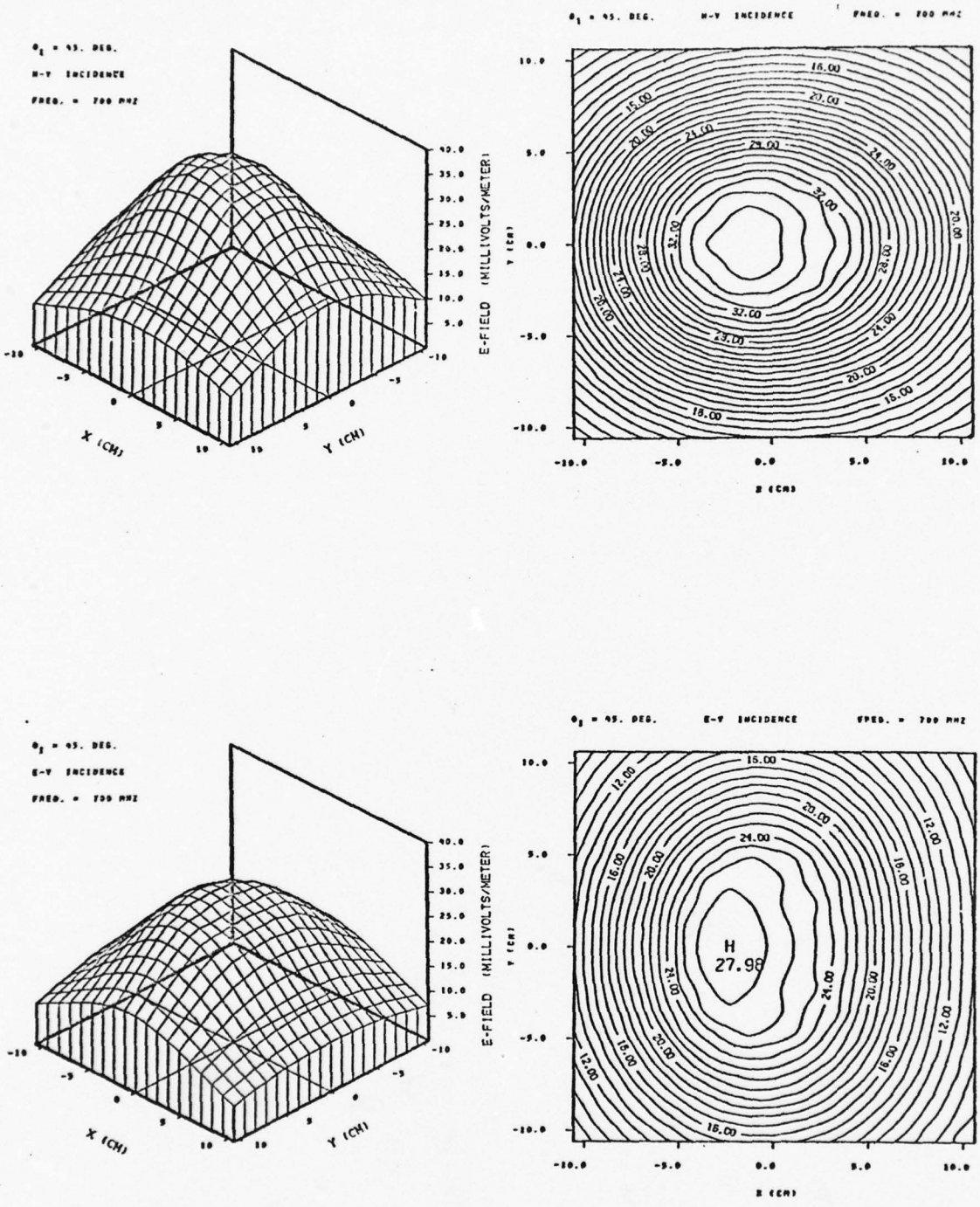

Figure 9. 3-D and contour plots os scattered E-field amplitude on the earth surface (θ_i = 45°, frequency = 700 MHz)

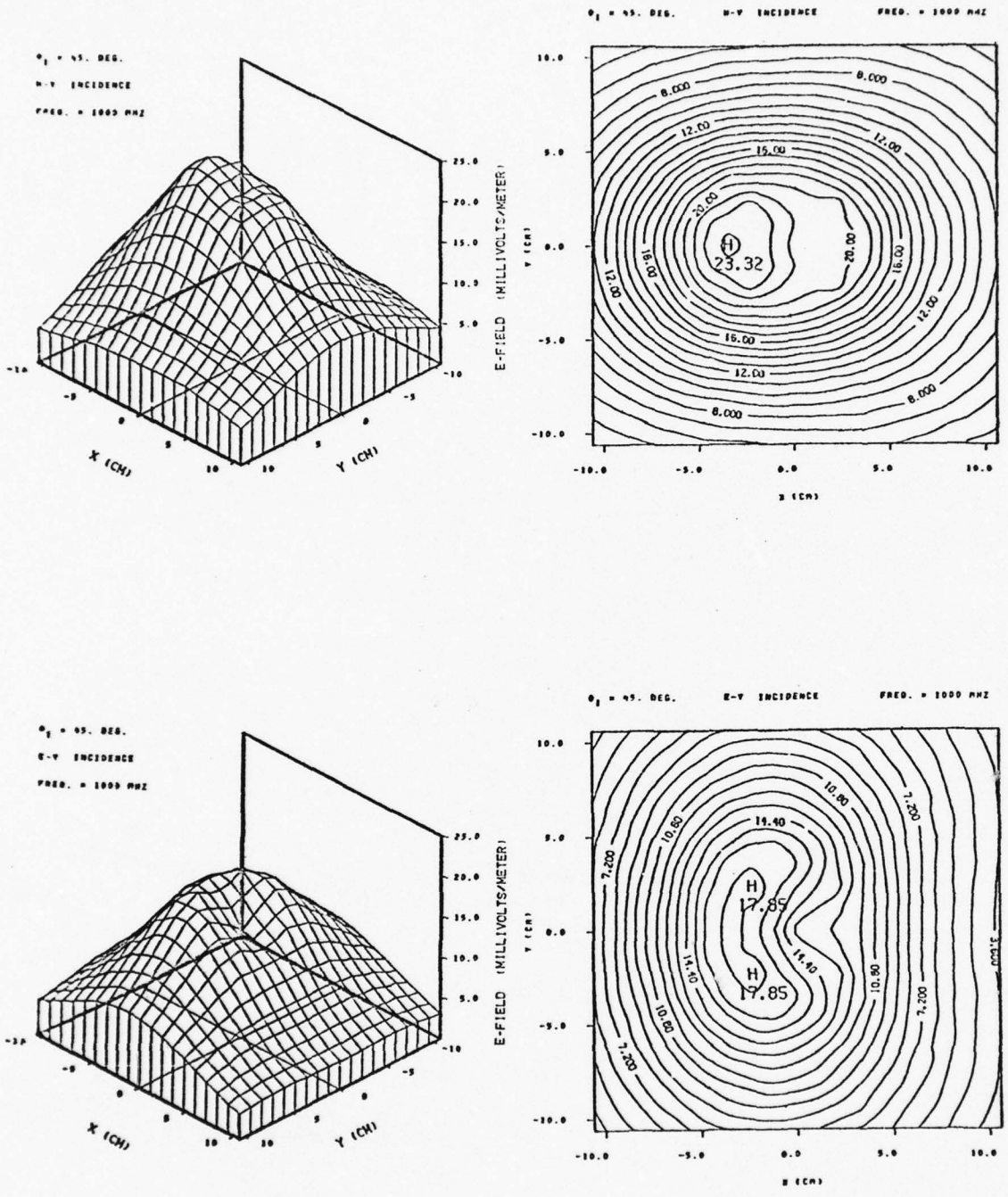

Figure 10. 3-D and contour plots of scattered E-field amplitude on the earth surface (θ_i = 45°, frequency = 1000 MHz)

over that of 700 MHz because of higher attenuations and change of scattering effects. An interesting phenomena also happens at this frequency, i.e., the central area is a local minimum while two peaks appeared near the rim of the mine position. The peaks locate on the x-axis for H-Y incidence and on the y-axis for E-Y incidence. This implies that the measurement of E-field amplitude along the line passing through the central point and parallel to the $\vec{E}$ vector will provide larger response.

Figures 9 and 10 are for $\theta_i = 45°$ at 700 MHz and 1000 MHz, respectively. It is seen on these figures that the peak values have shifted toward the negative direction because the incident waves are coming from the positive x. The fields are symmetric against the x axis, owing to the symmetries of the mine geometry.

(2) θ_i parametric studies

Figure 11 shows the scattering configuration and the lines on which the scattered E-fields are to be plotted. Figures 11a and 11b are for the H-Y incidence, and 11c and 11d for the E-Y incidence. Figures 11a and 11c indicate the line sections parallel to the x-axis on which the fields are to be plotted. Figures 11b and 11d show the similar lines parallel to the y-axis. Figure 11 is the reference for all of the results to be presented in Figures 12-27.

Figure 12 shows the results at 700 MHz on the ground surface. As the angle θ_i increases, the amplitude tends to decrease accordingly. This is because less energy is transmitted into the ground when θ_i is larger. The peak along x has shifted leftward when θ_i is not equal to zero. In general, the peak values of H-Y incidence are higher than those of E-Y incidence especially when θ_i is large.

Figures 13-15 show the results at 800 MHz, 900 MHz, and 1000 MHz, respectively. The E-fields near the center ($x = 0$, $y = 0$) at these frequencies are local minima. The peaks appear at about $3 \sim 4$ cm from the center depending on the frequency. Along the x direction, at oblige incidences, the peaks on the right side are depressed, and those on the left are enhanced. The curves along the y direction are all symmetric to $y = 0$. For all frequencies, the E-Y incidence at oblige angles yield less scattered E-field than the H-Y incidence.

(3) Frequency parametric studies

Figures 16 and 17 show the frequency parametric studies for the E-field on the ground ($z = 0$) with $\theta_i = 0°$ and $45°$, respectively. These figures indicate the trend that the scattering amplitude is larger when the frequency is lower. However, the response at low frequency, 700 MHz, the patterns tend to be flattened. At higher frequencies, special characteristics such as a dip near the center and the maxima at near $3 \sim 4$ cm from the center have become apparent. These may be useful for engineers in designing the detection systems.

(4) z parametric studies

From Figures 18 through 37, the results are displayed for all $\theta_i = 0°$, $30°$, $45°$, $60°$, $75°$, each with two incident polarizations, and $f = 700$ MHz, 800 MHz, 900 MHz, 1000 MHz. The scattering values for each case at $z = 0$ cm, 2.54 cm, 5.08 cm, 7.62 cm, and 12.70 cm are shown in the same figure so that the trend of the height of measurements can be seen easily.

For the design of mine detection systems, it is important to know the height and position of the measurement. The z parametric studies all show that the scattered E-fields taper off at large x, y and z values. The peak scattered field at $z = 12.7$ cm generally reduce to about $10 \sim 25\%$ of the peak values on the ground. Hence it is desirable to measure the fields as close to the ground as possible.

At frequencies higher than 700 MHz, the field patterns on the ground all show that the maxima have shifted off the center point above the mine. However, this type of anomaly disappears at $z = 2.5$ cm and higher.

It is expected that the numerical results presented in this section will be found useful for engineers and technical staff in understanding the electromagnetic phenomena of the buried dielectric land mines so that an efficient mine detection system can be designed and improved.

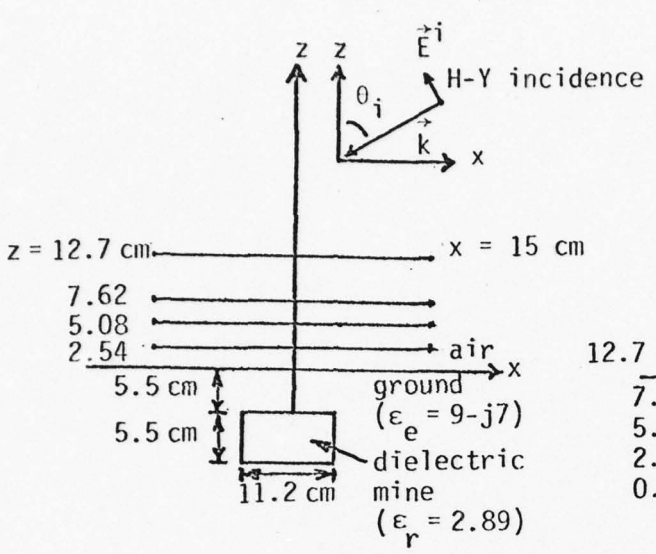

(a) H-Y incidence; scattered field to be shown on lines parallel to x.

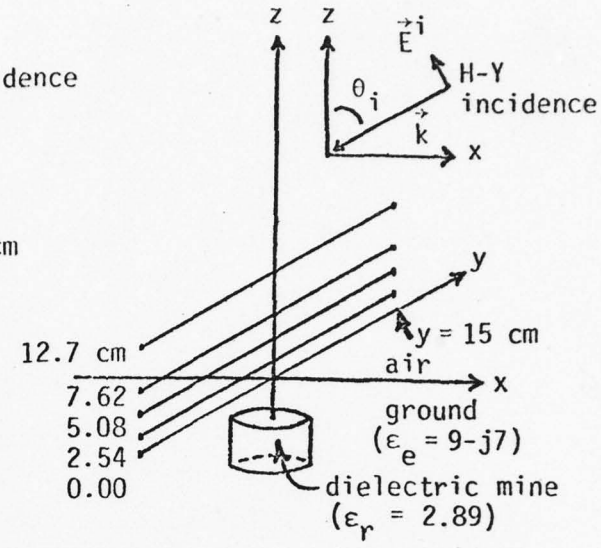

(b) H-Y incidence; scattered field to be shown on lines parallel to y.

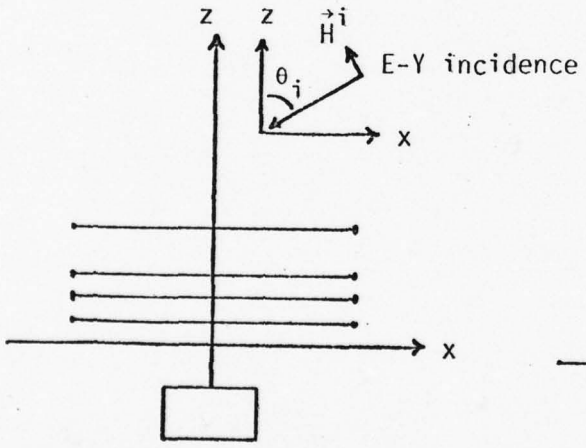

(c) E-Y incidence; scattered field to be shown on lines parallel to x.

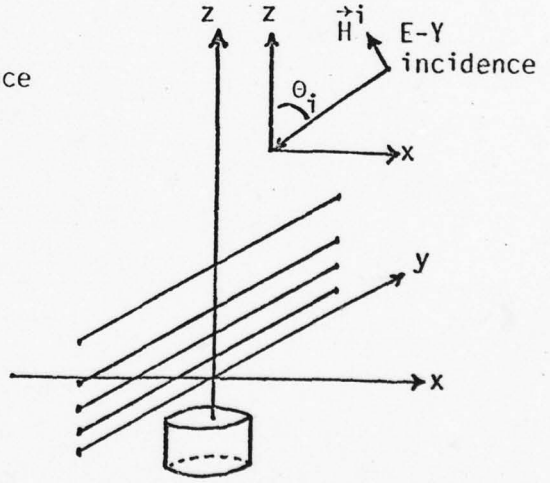

(d) E-Y incidence; scattered field to be shown on lines parallel to y.

Figure 11. Four illustrations of the land mines, the incident waves, and the lines on which the scattered electric fields will be shown

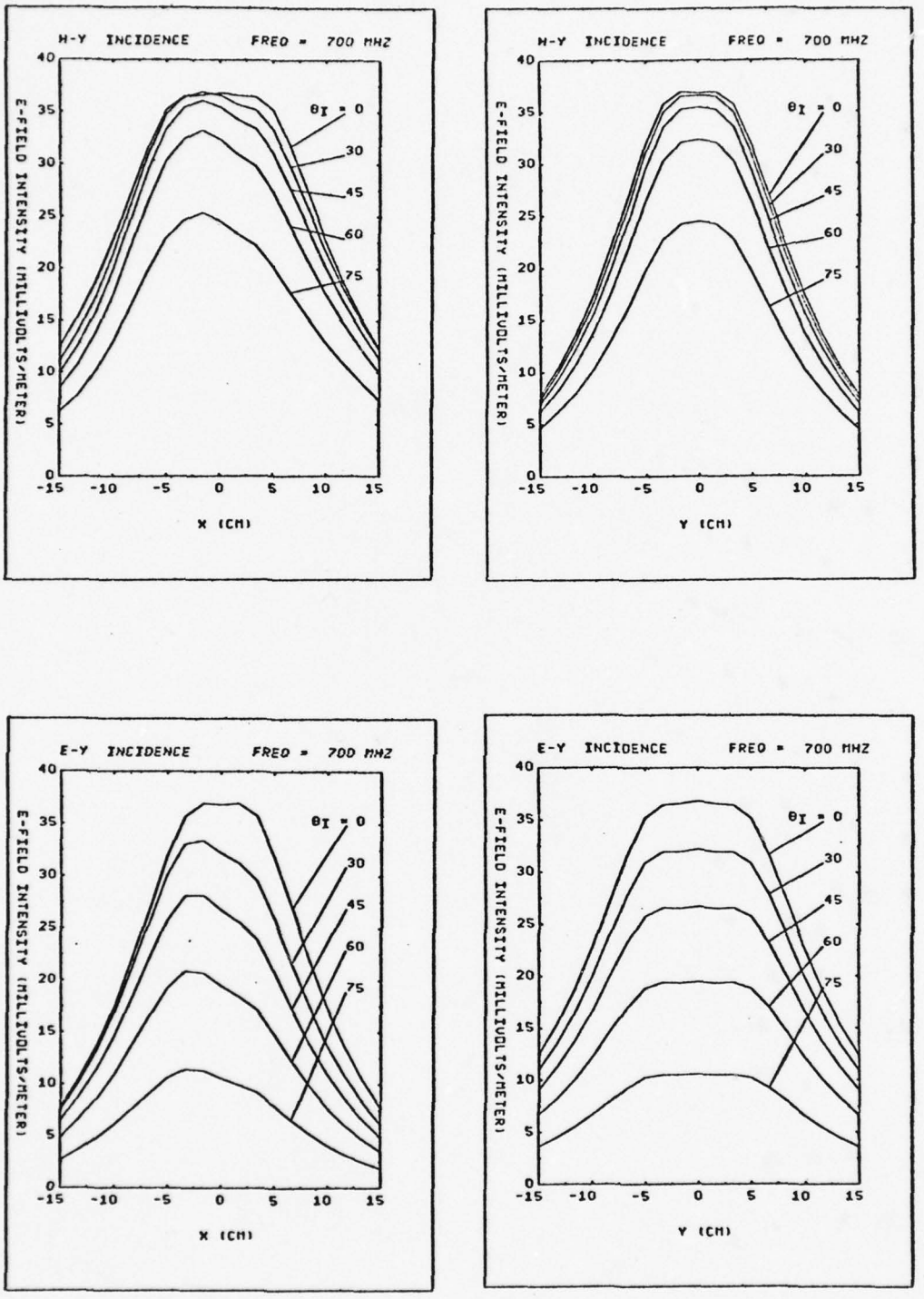

Figure 12. Parametric curves of incident angles for scattered E-field on the earth surface (z = 0) at frequency = 700 MHz

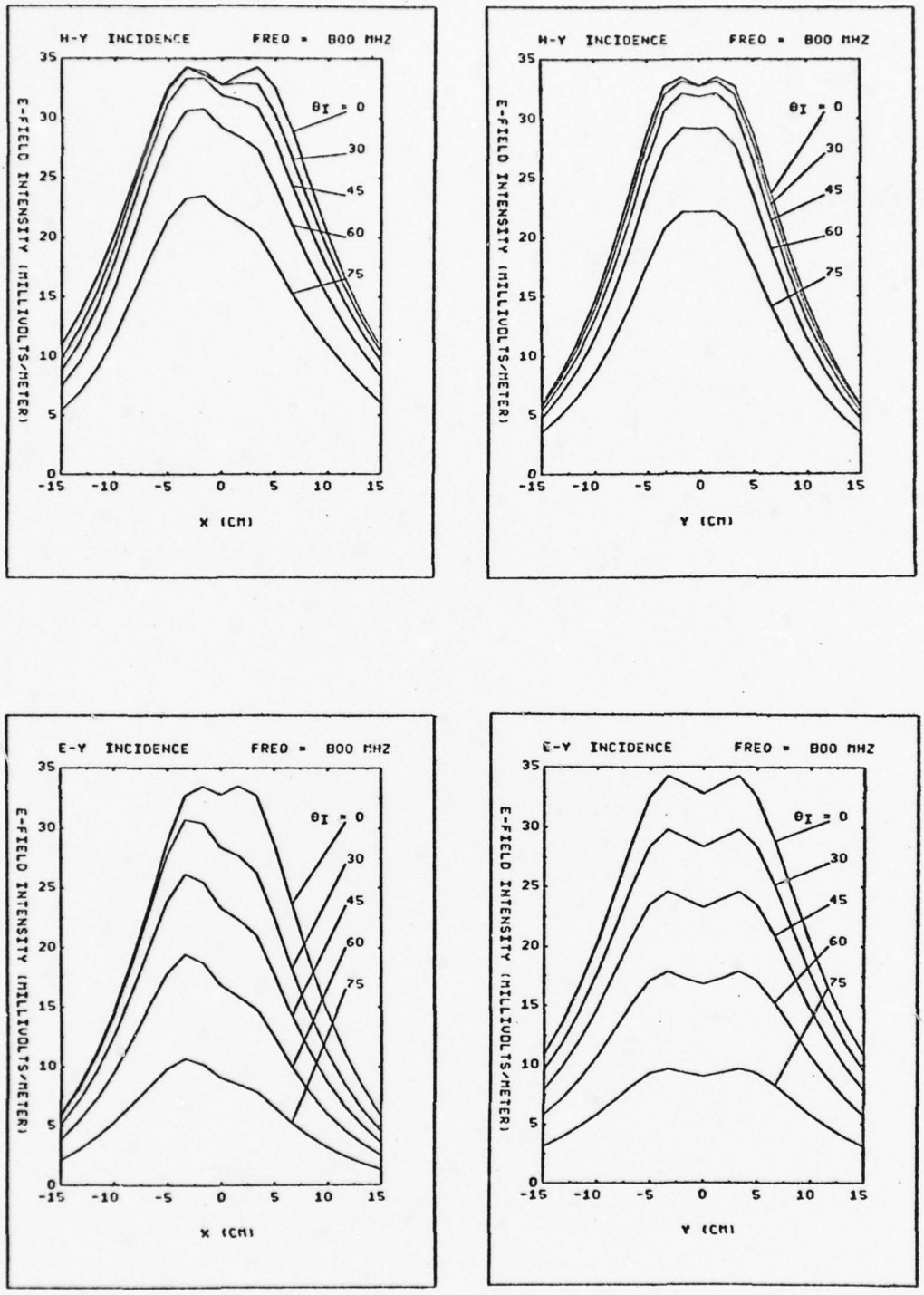

Figure 13. Parametic curves of incident angles for scattered E-Field on the earth surface (z = 0) at frequency = 800 MHz

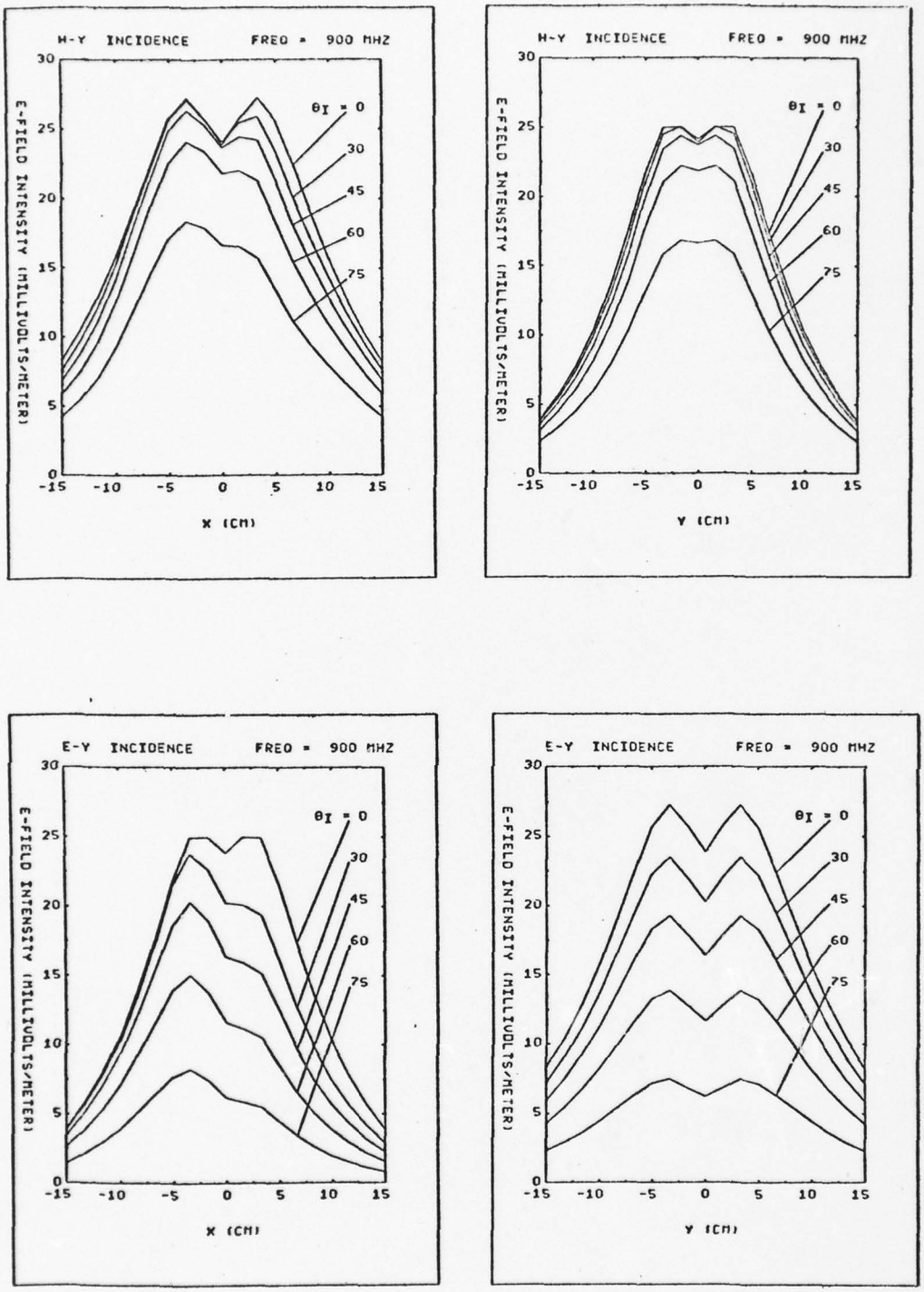

Figure 14. Parametric curves of incident angles for scattered E-field on the earth surface (z = 0) at frequency = 900 MHz

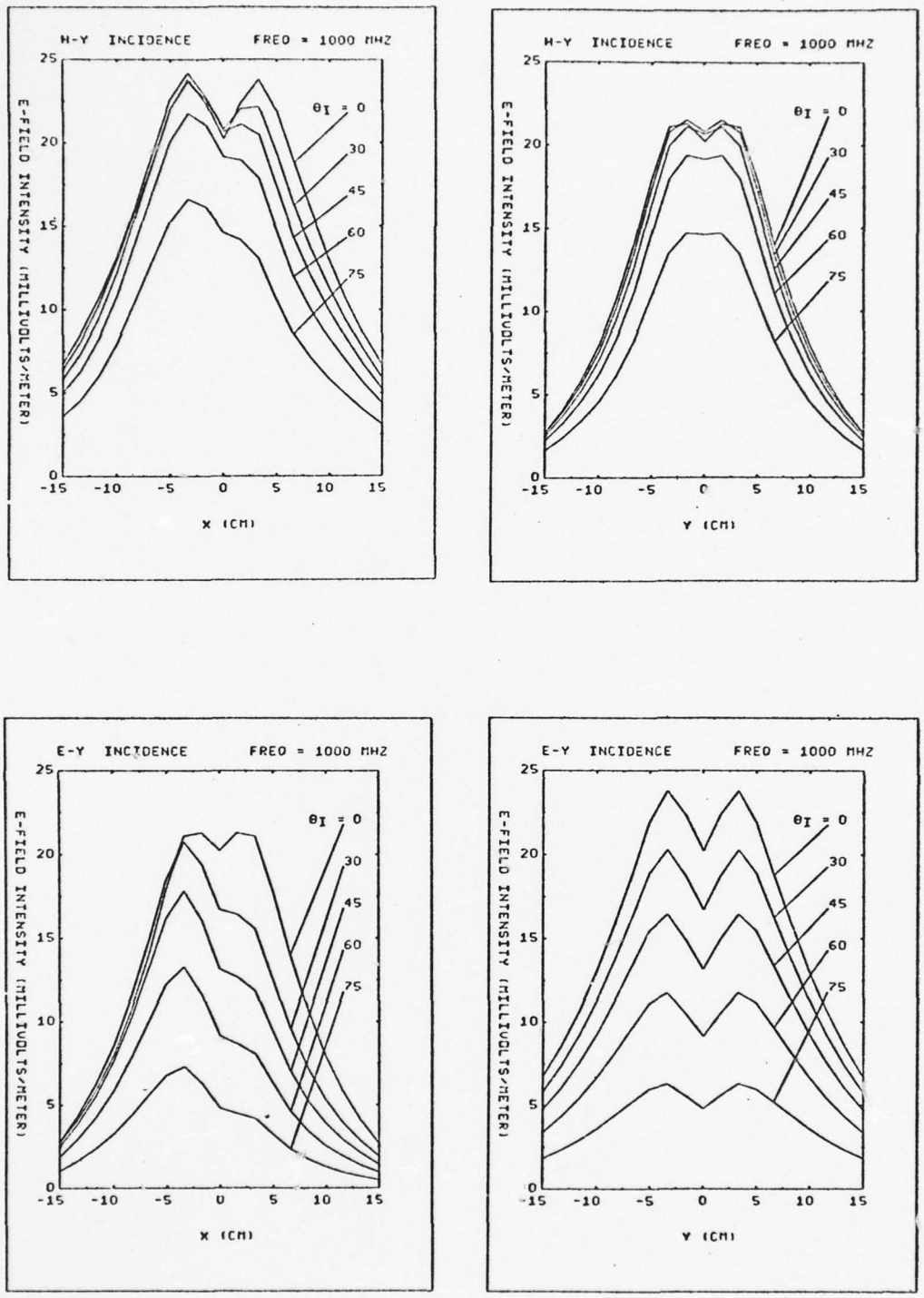

Figure 15. Parametric curves of incident angles for scattered E-field on the earth surface (z = 0) at frequency = 1000 MHz

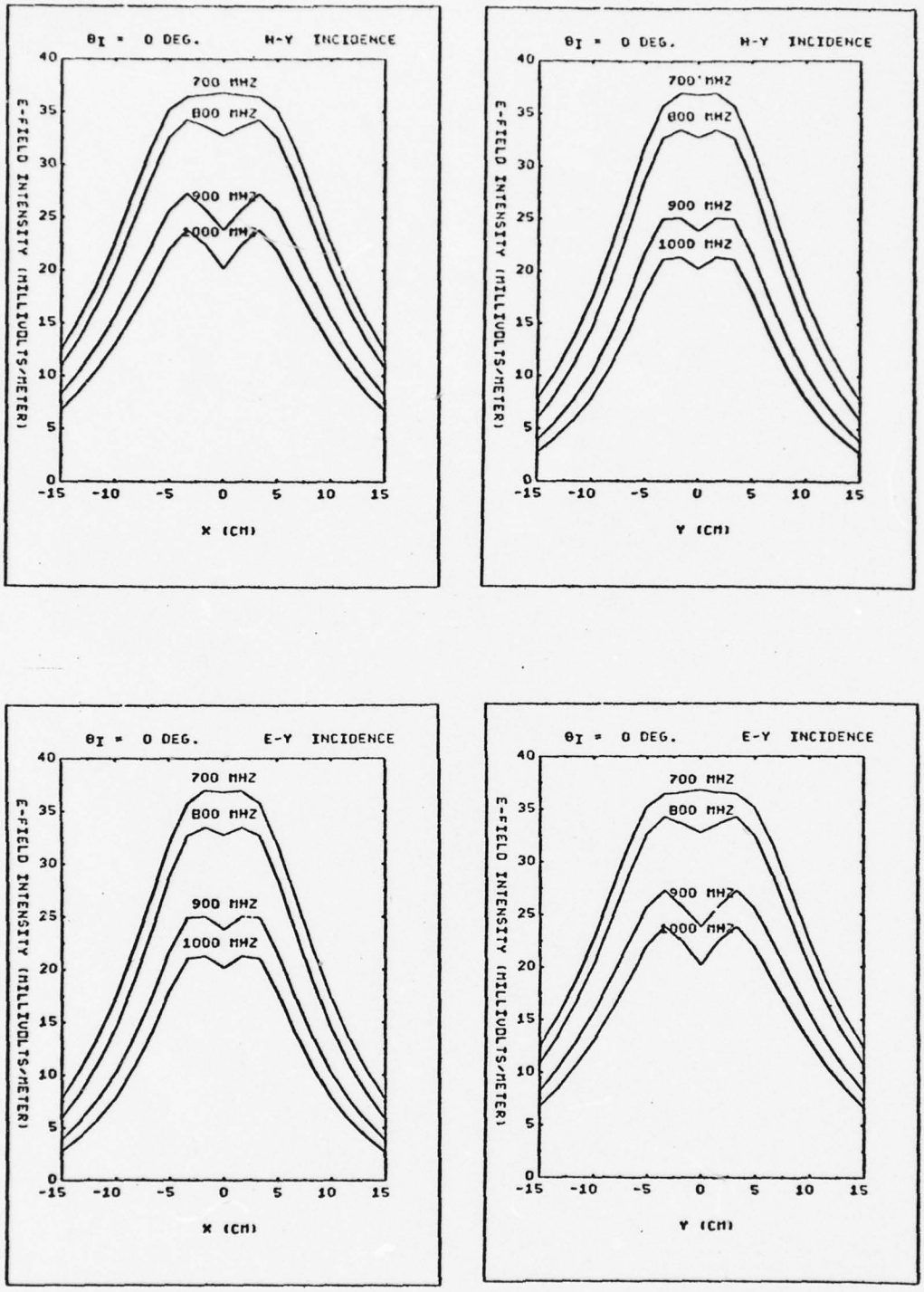

Figure 16. Parametric curves of frequency for the scattered E-field on the earth surface ($z = 0$) with incident angle $\theta_i = 0°$

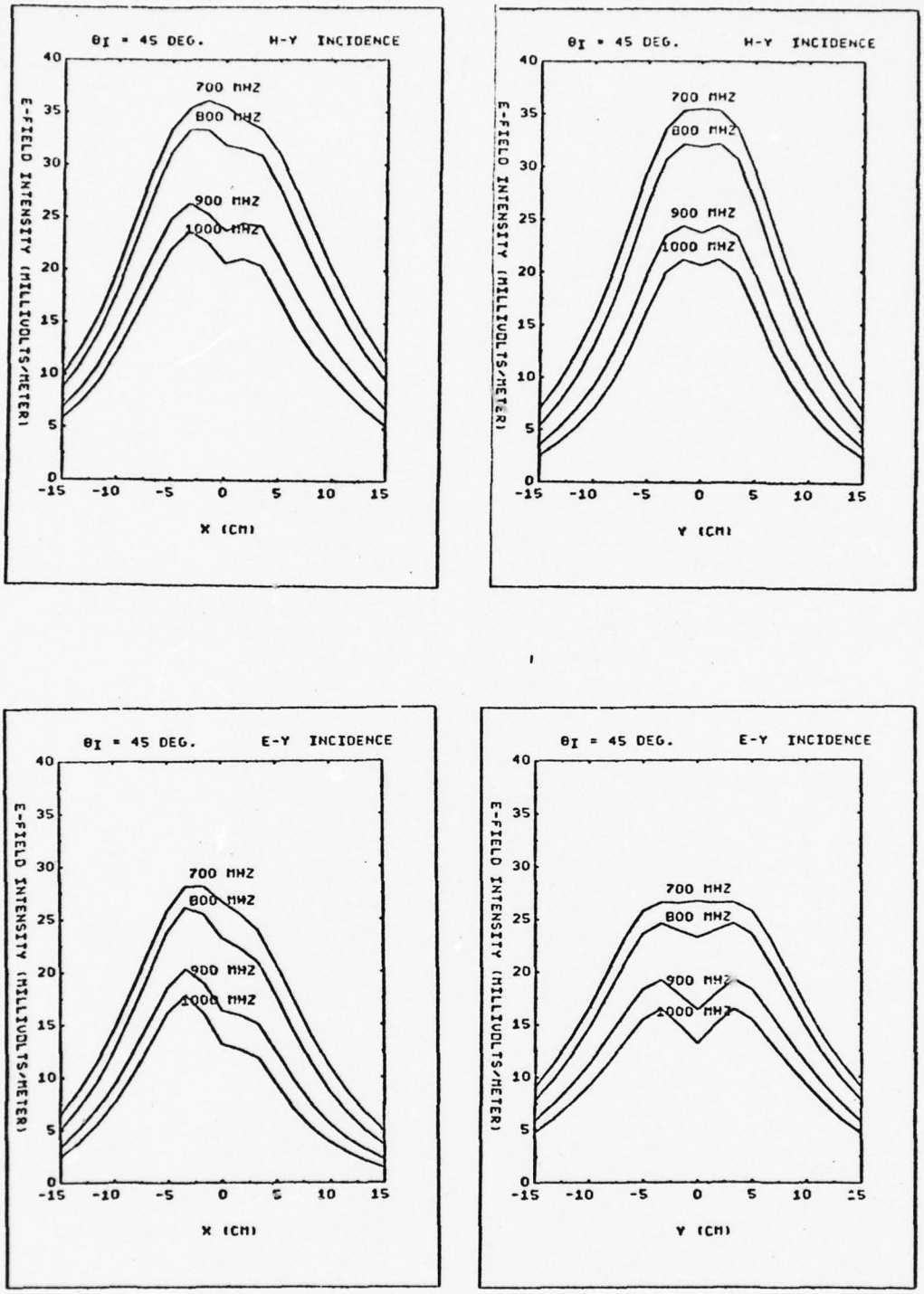

Figure 17. Parametric curves of frequency for the scattered E-field on the earth surface ($z = 0$) with incident angle $\theta_i = 45°$

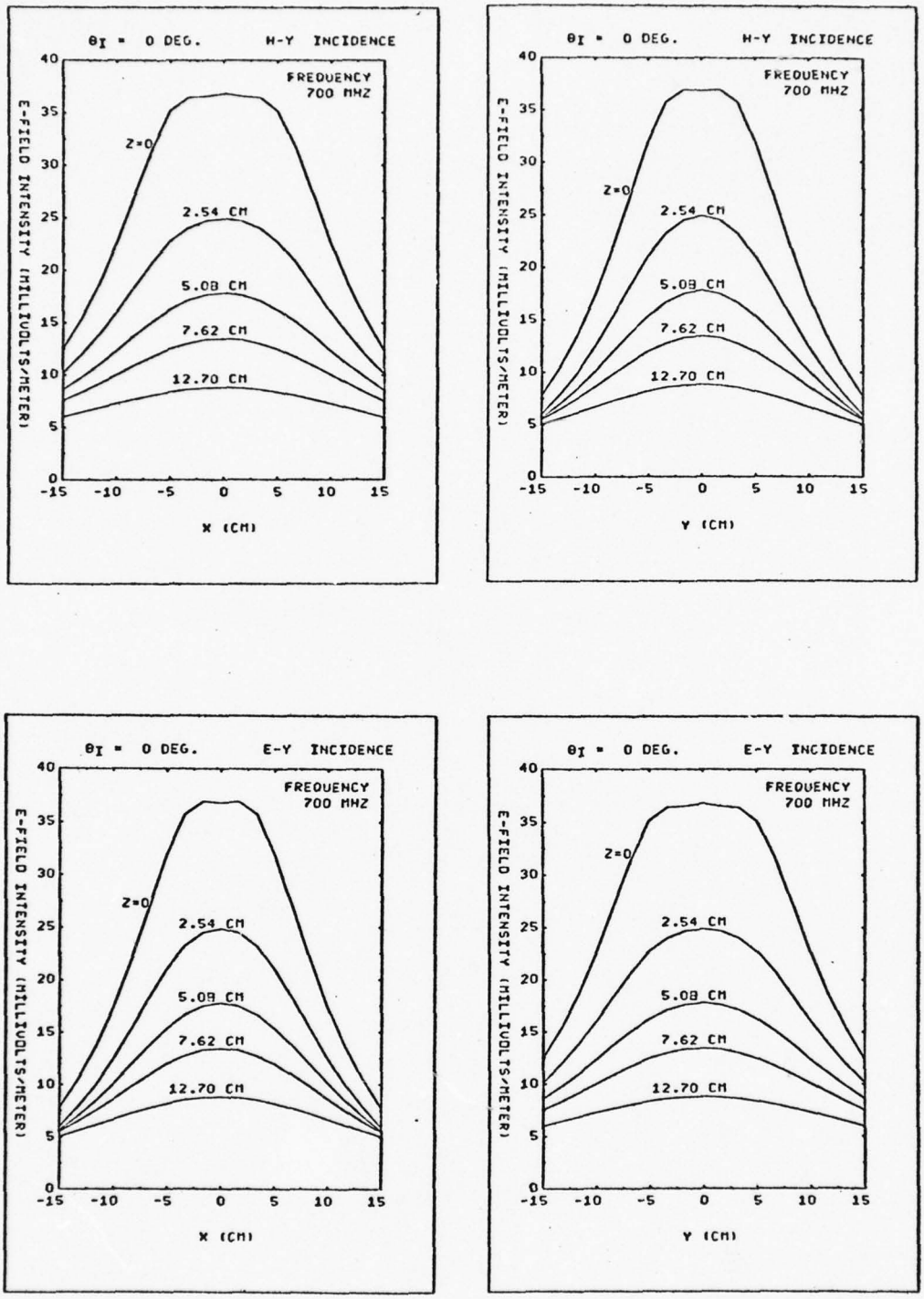

Figure 18. Parametric curves of z for the scattered E-field for incident angle $\theta_i = 0°$ at frequency = 700 MHz

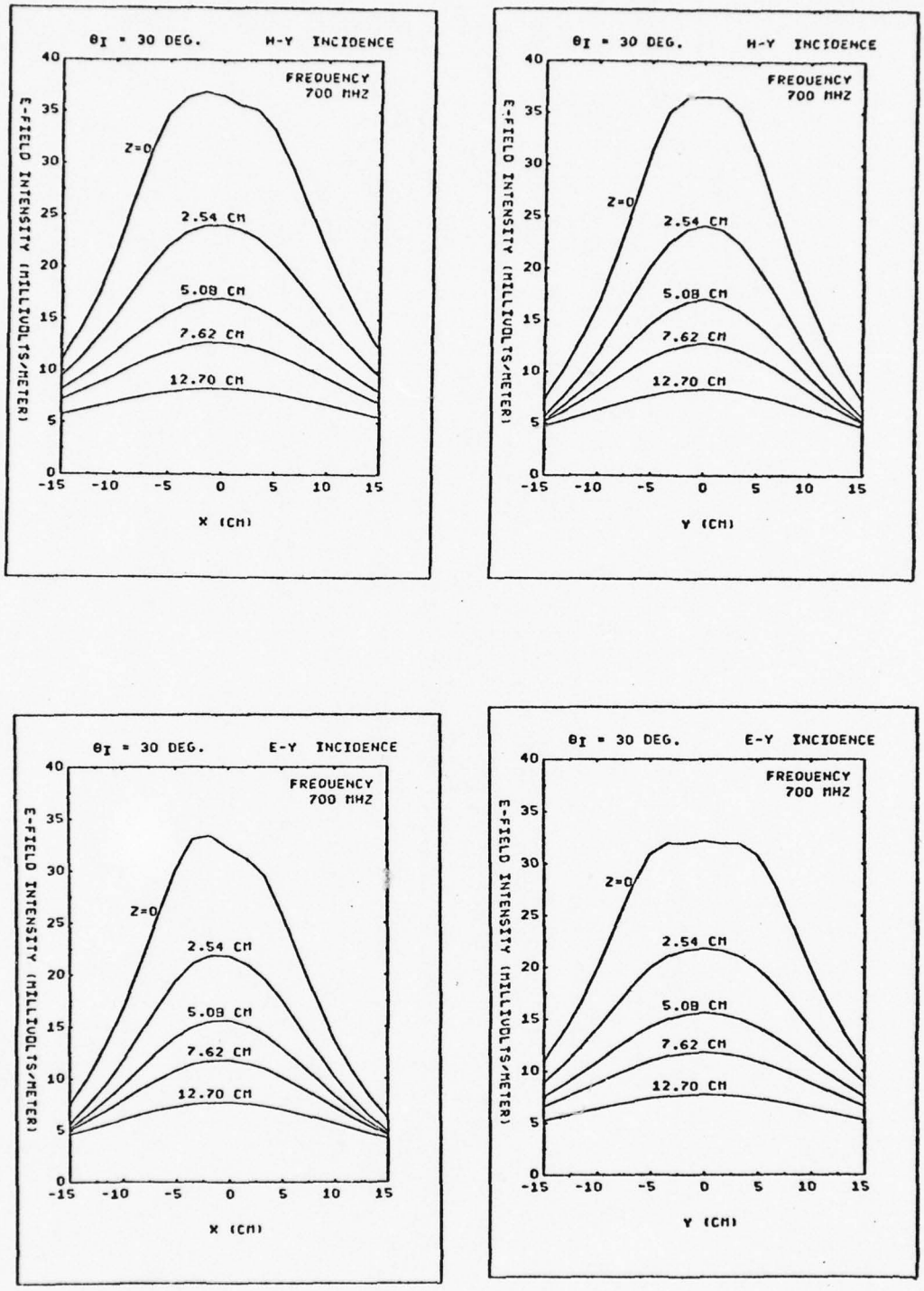

Figure 19. Parametric curves of z for the scattered E-field for incident angle θ_i = 30° at frequency = 700 MHz

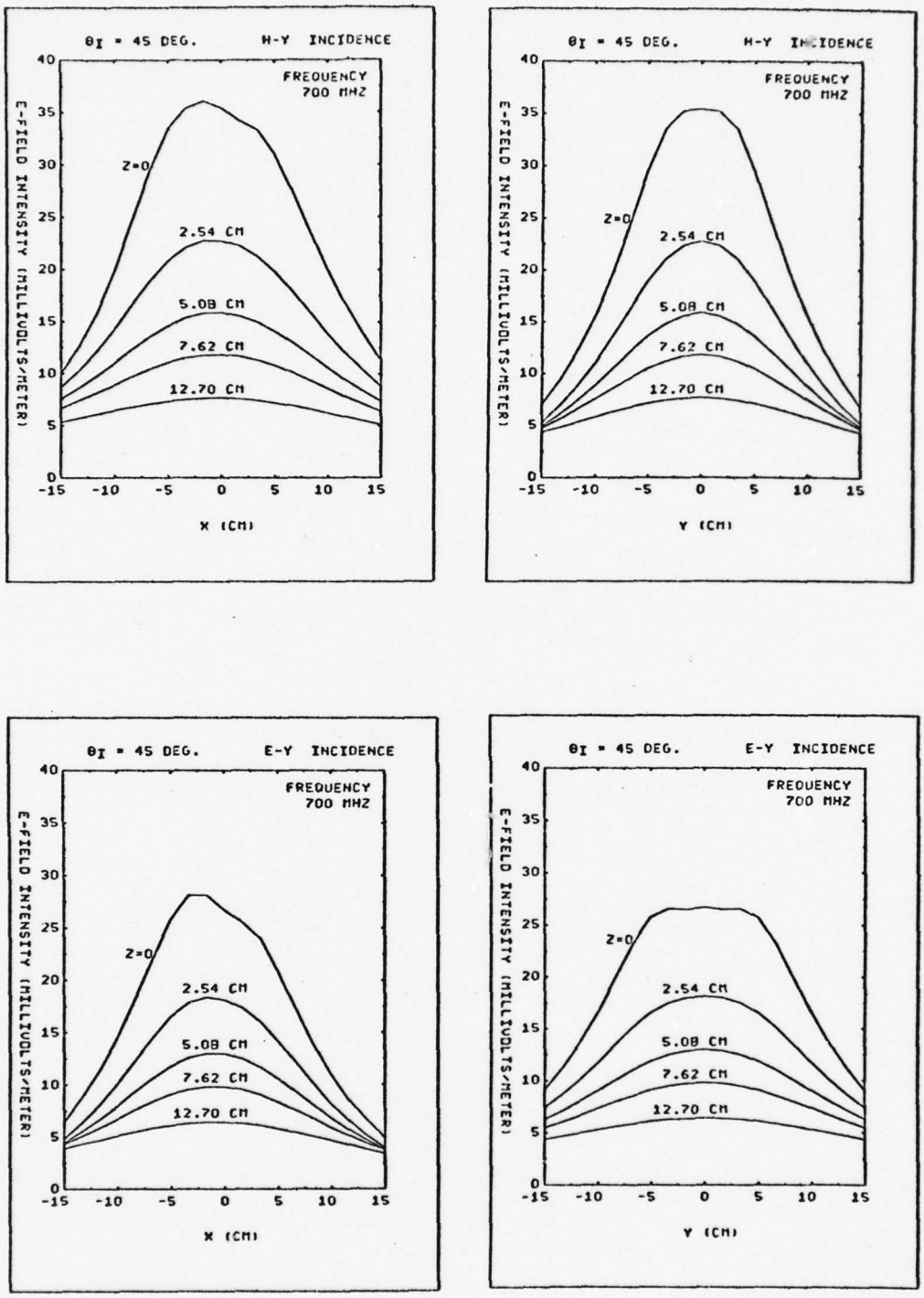

Figure 20. Parametric curves of z for the scattered E-field for incident angle θ_i = 45° at frequency = 700 MHz

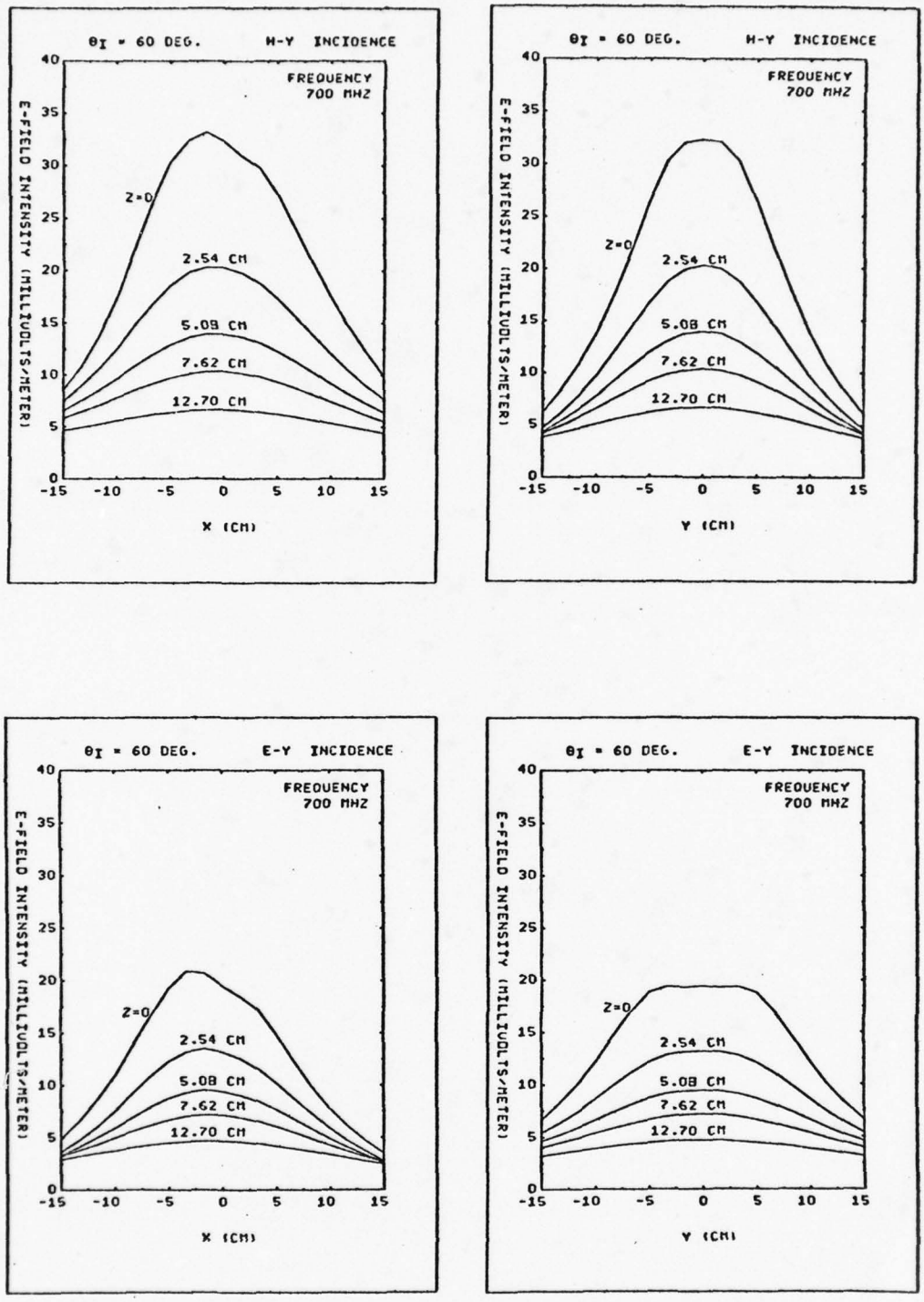

Figure 21. Parametric curves of z for the scattered E-field for incident angle $\theta_i = 60°$ at frequency = 700 MHz

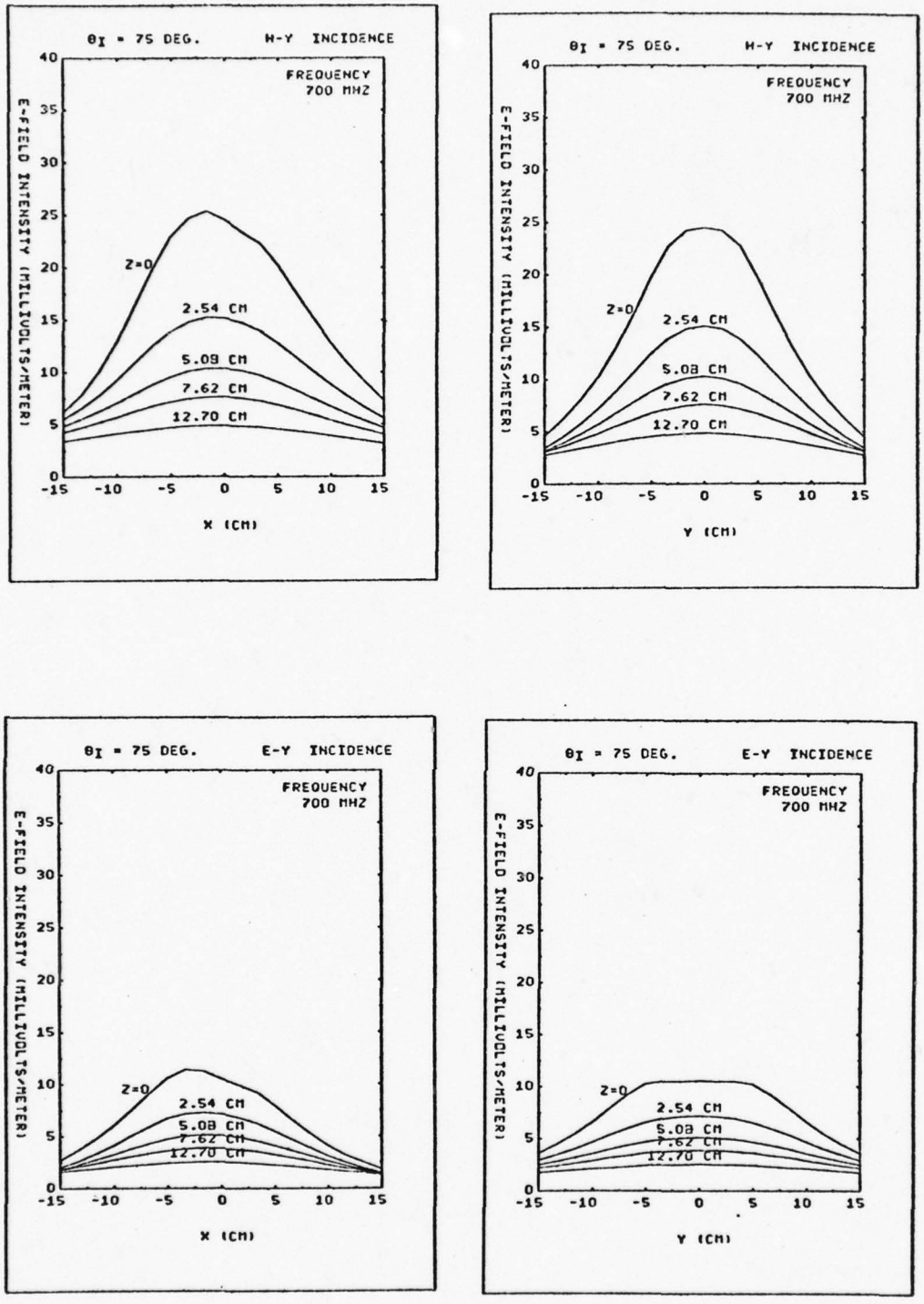

Figure 22. Parametric curves of z for the scattered E-field for incident angle θ_i = 75° at frequency = 700 Mhz

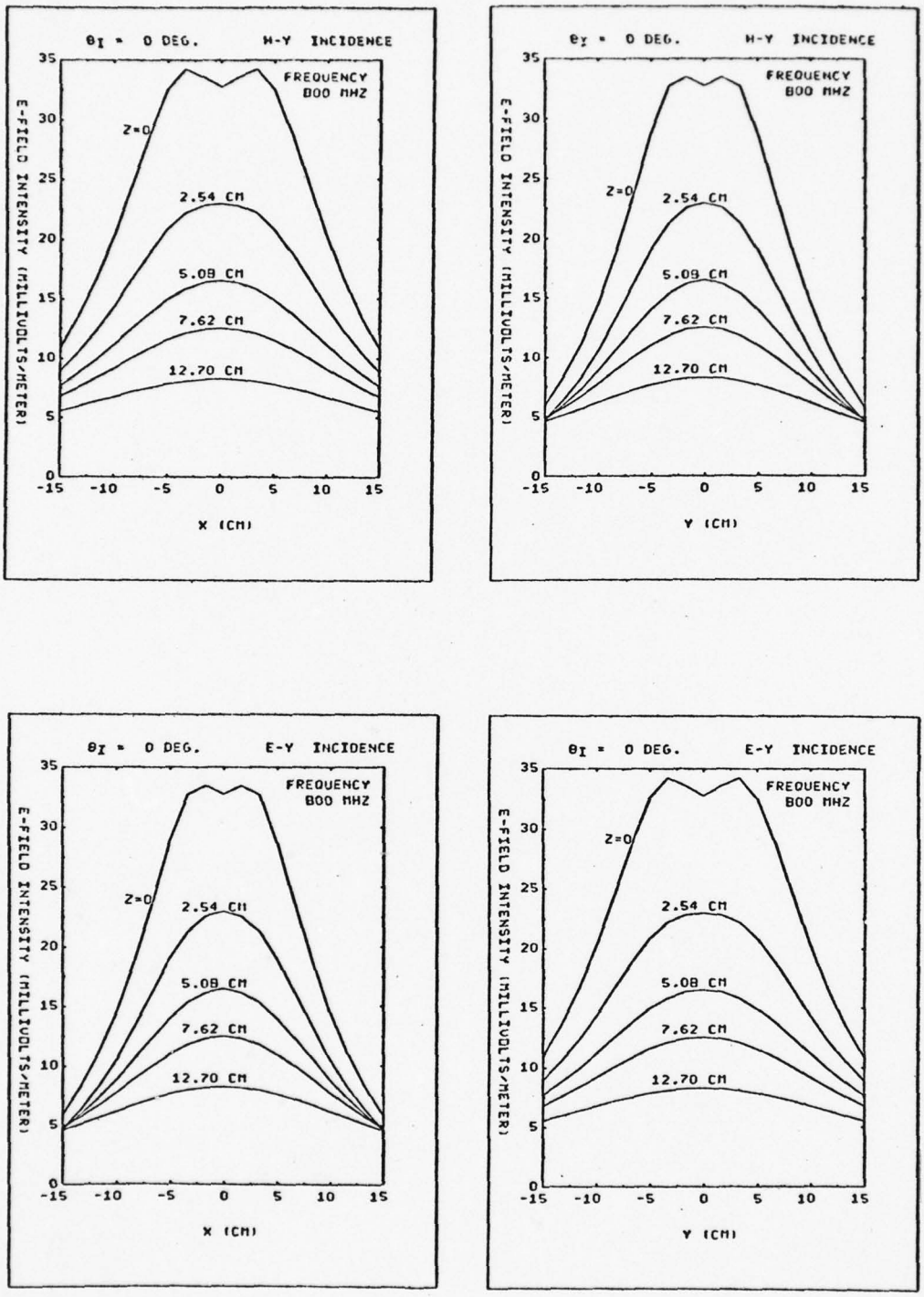

Figure 23. Parametric curves of z for the scattered E-field for incident angle $\theta_i = 0°$ at frequency = 800 MHz

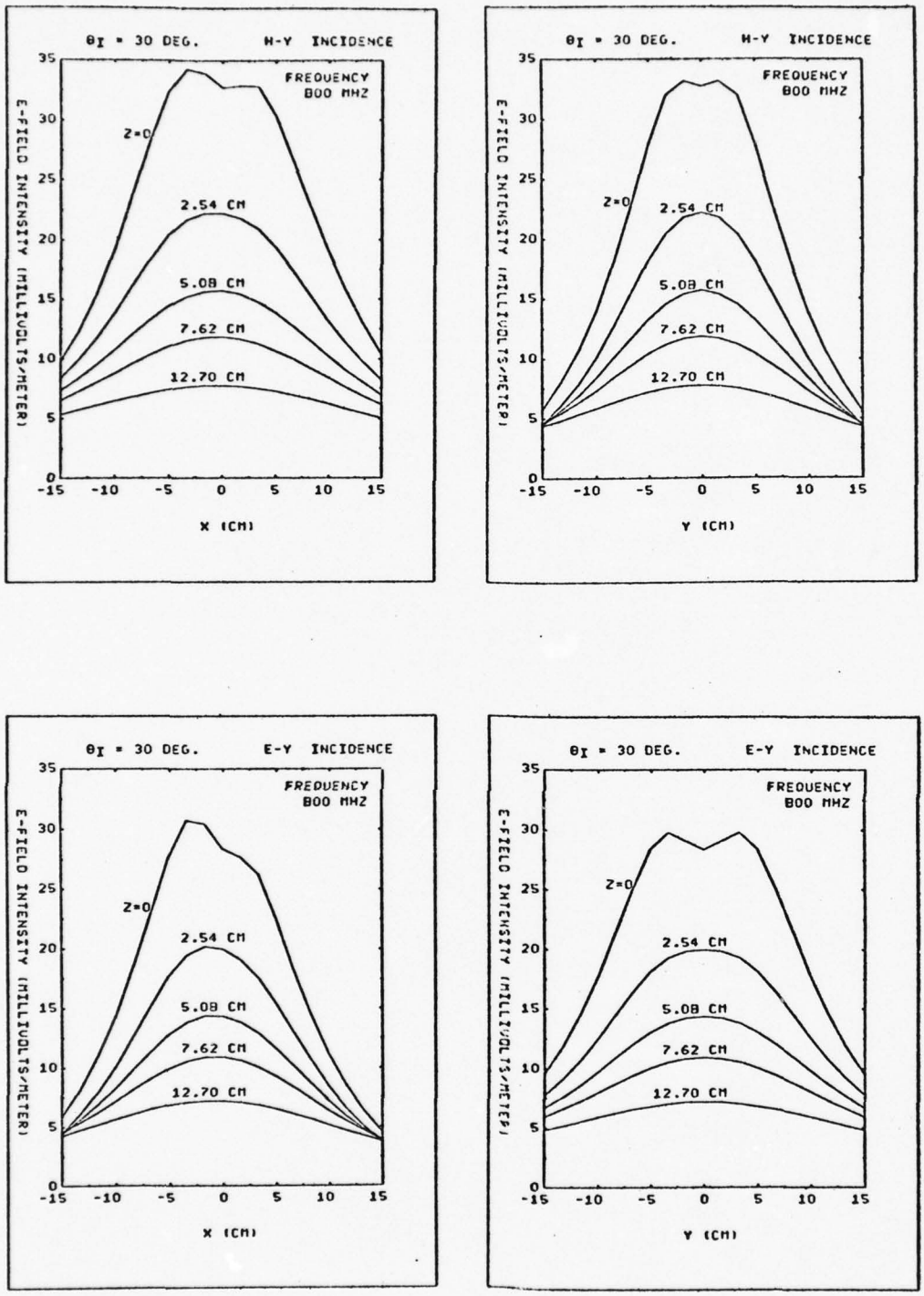

Figure 24. Parametric curves of z for the scattered E-field for incident angle θ_i = 30° at frequency = 800 MHz

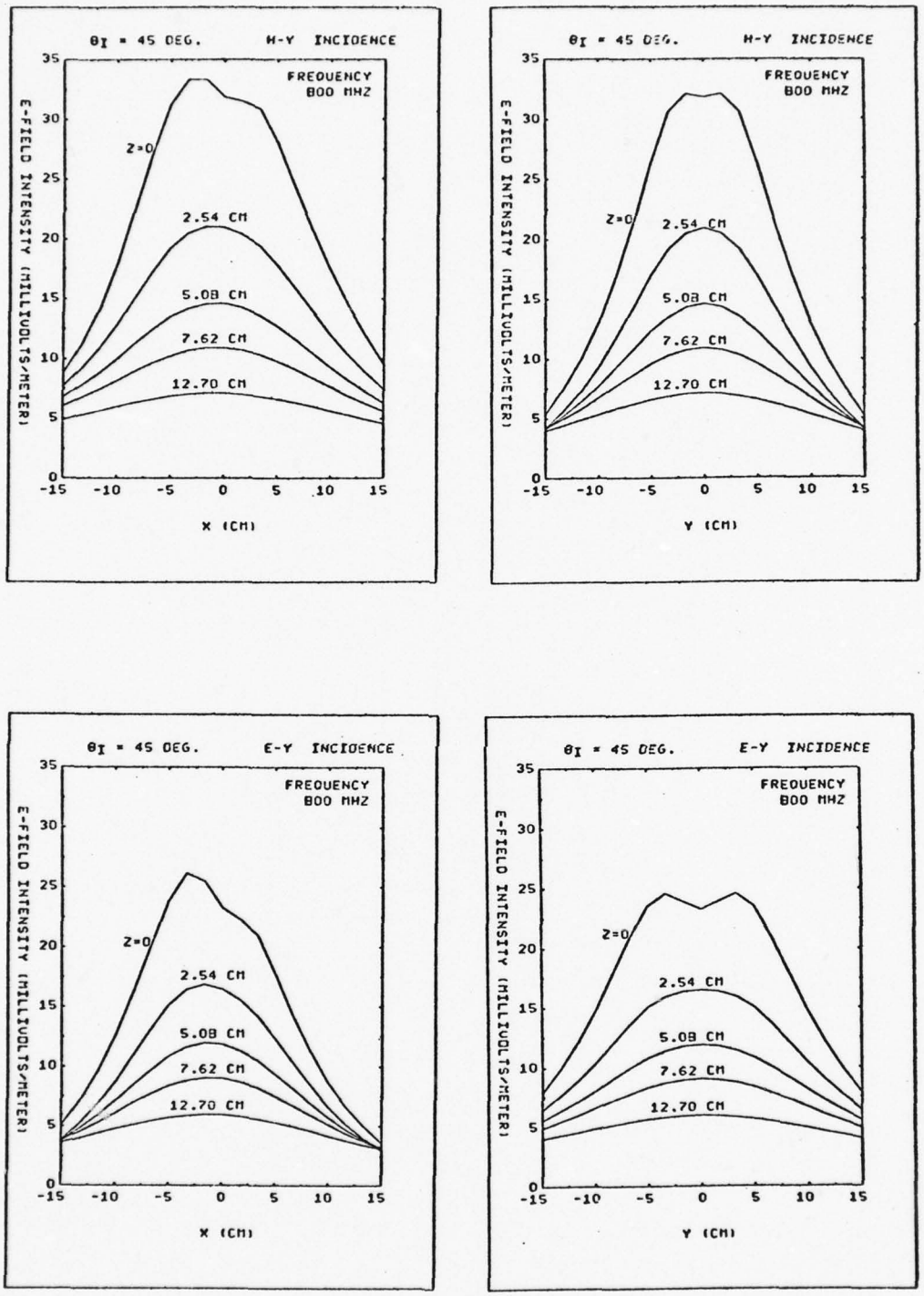

Figure 25. Parametric curves of z for the scattered E-field for incident angle $\theta_i = 45°$ at frequency = 800 MHz

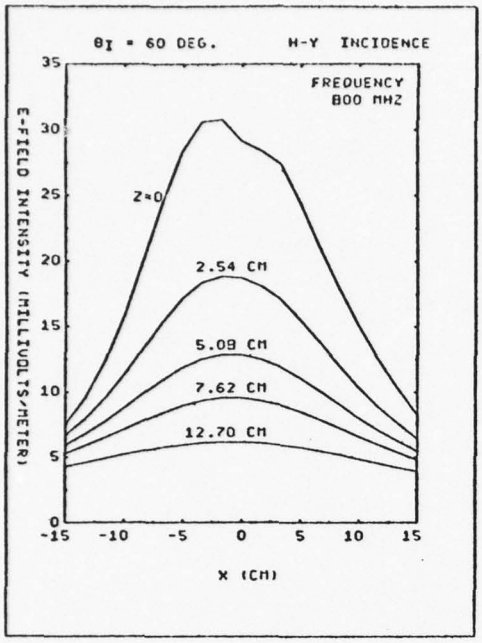

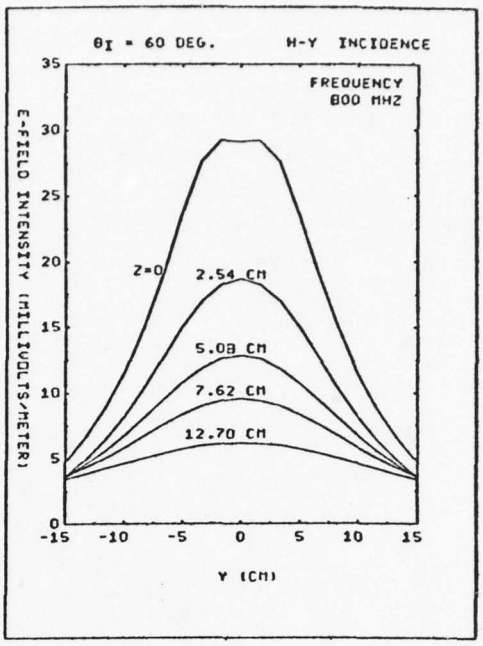

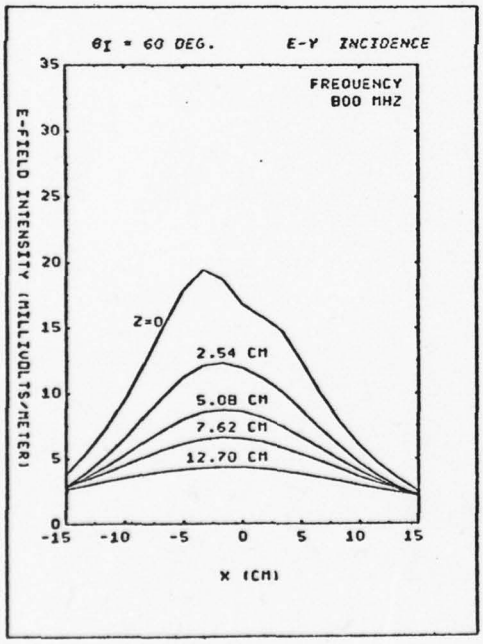

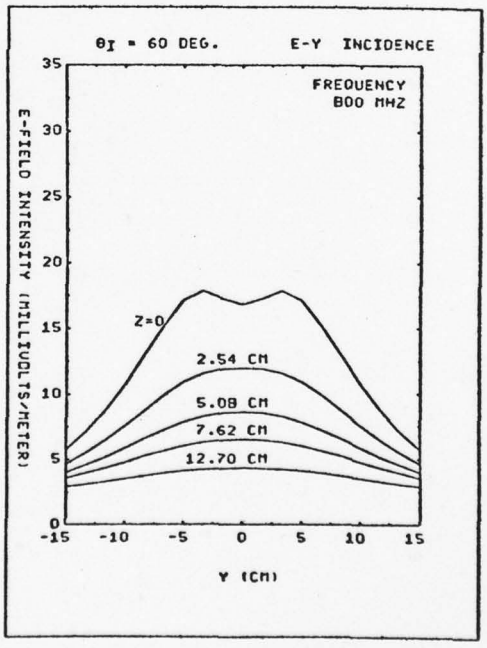

Figure 26. Parametric curves of z for the scattered E-field for incident angle $\theta_i = 60°$ at frequency = 800 MHz

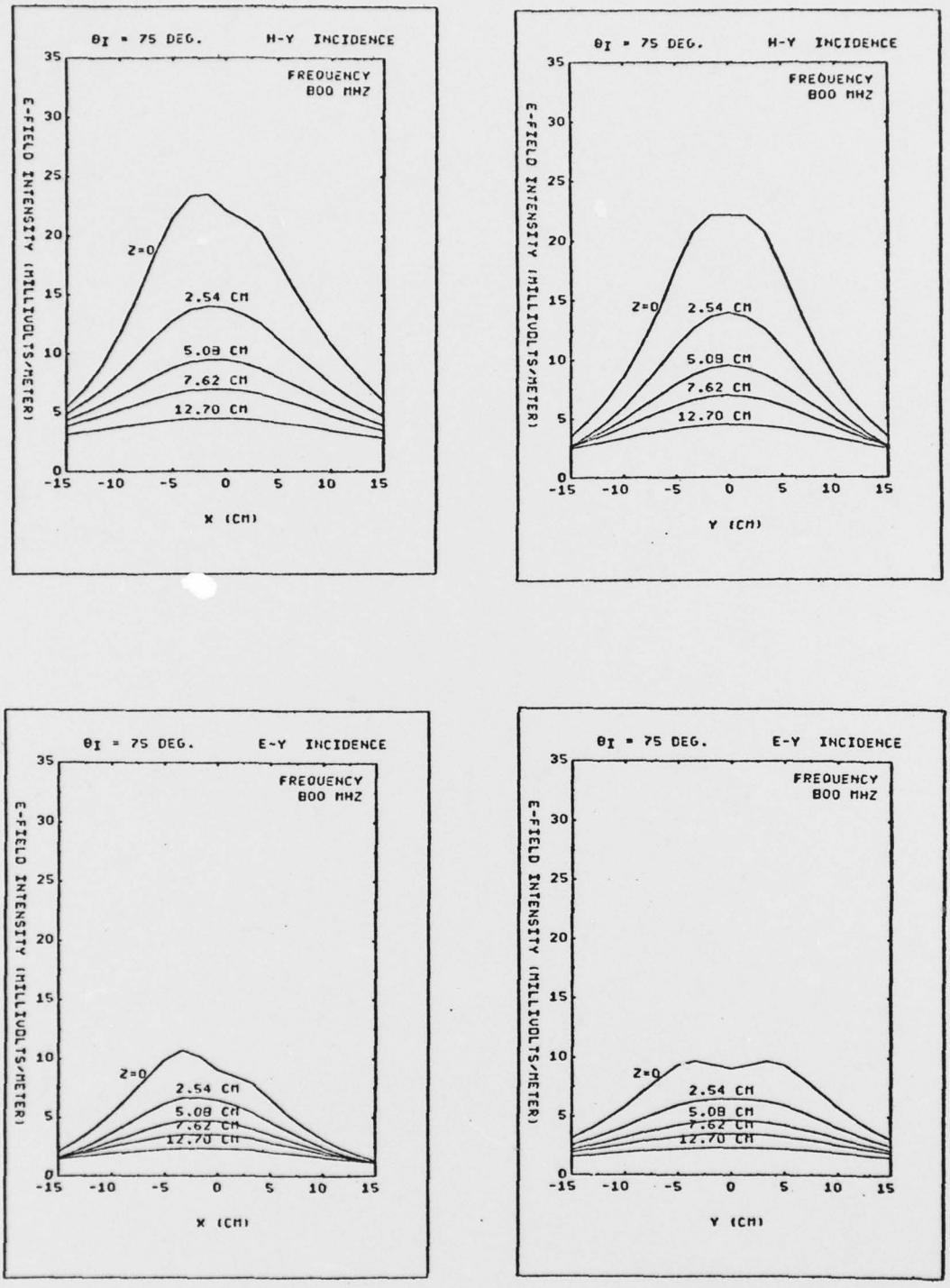

Figure 27. Parametric curves of z for the scattered E-field for incident angle $\theta_i = 75°$ at frequency = 800 MHz

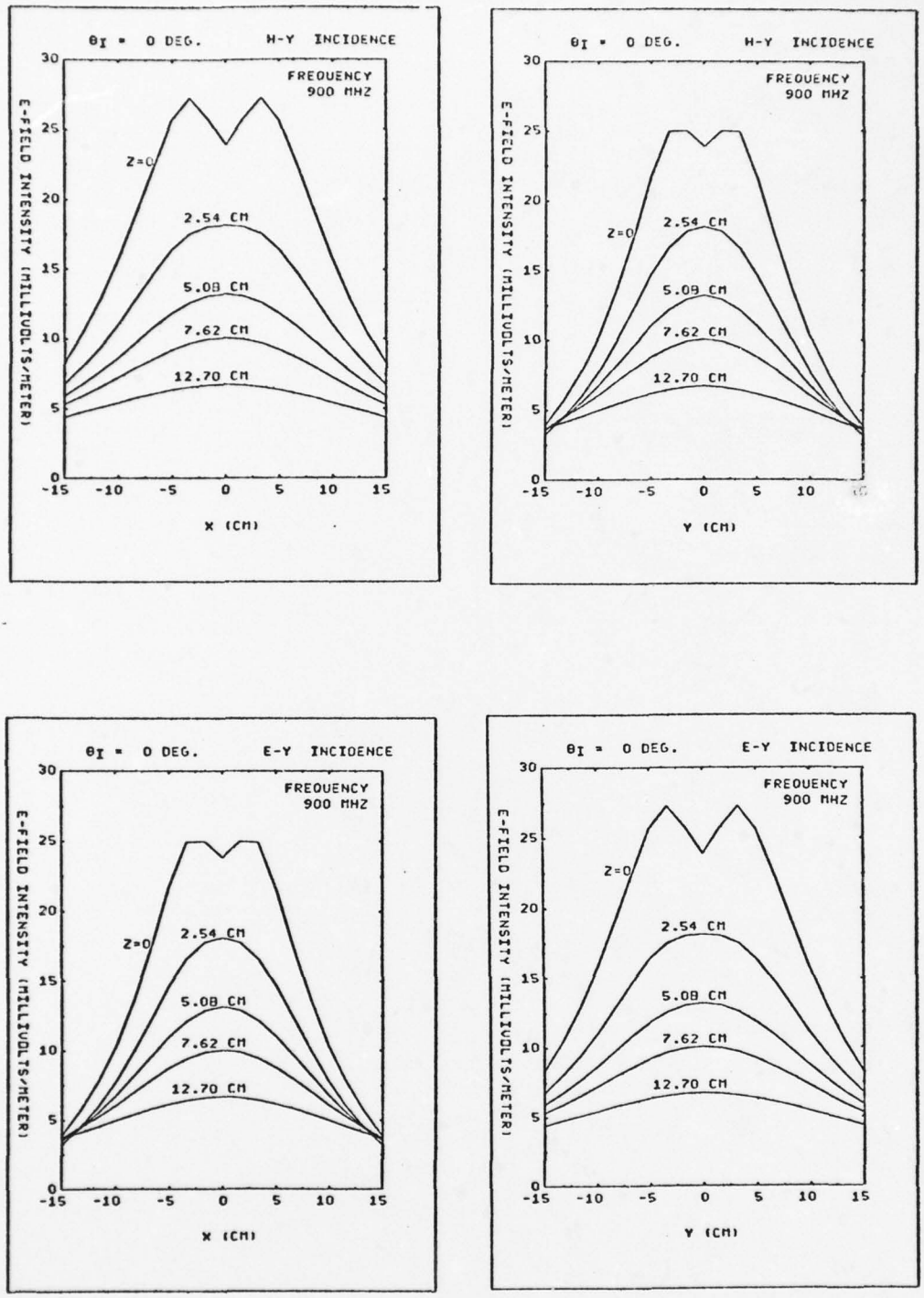

Figure 28. Parametric curves of z for the scattered E-field for incident angle $\theta_i = 0°$ at frequency = 900 MHz

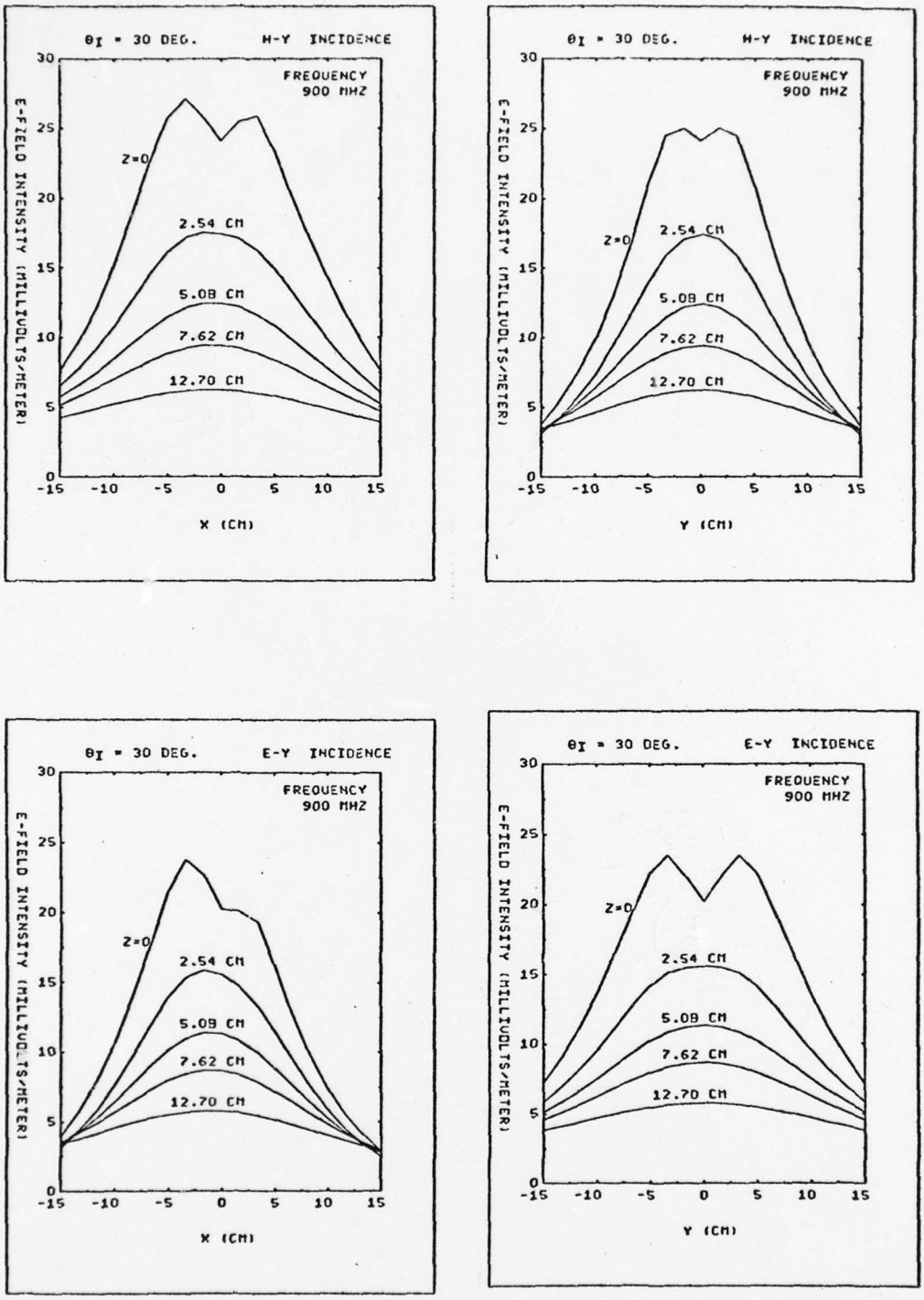

Figure 29. Parametric curves of z for the scattered E-field for incident angle $\theta_i = 30°$ at frequency = 900 MHz

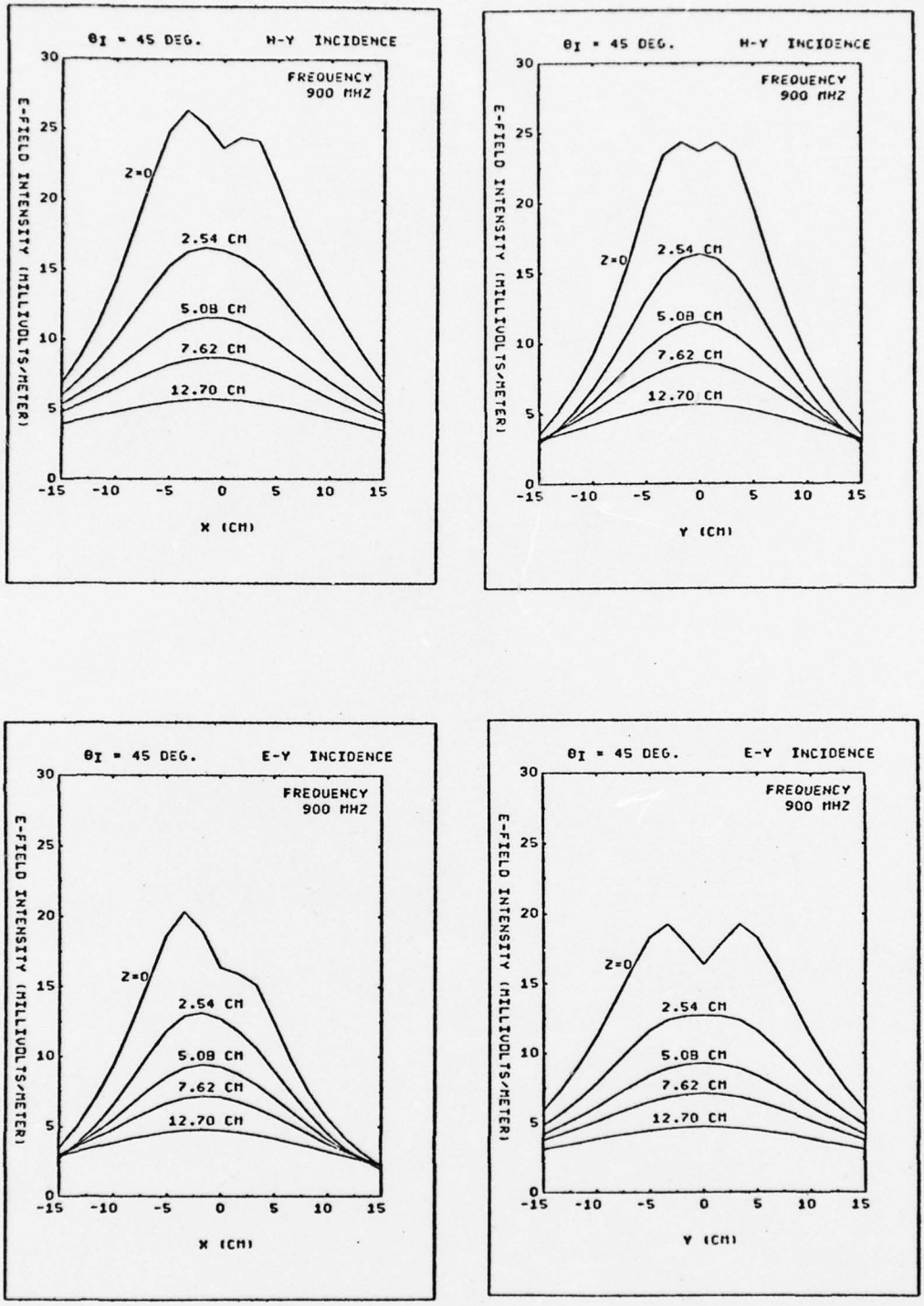

Figure 30. Parametric curves of z for the scattered E-field for incident angle $\theta_i = 45°$ at frequency = 900 MHz

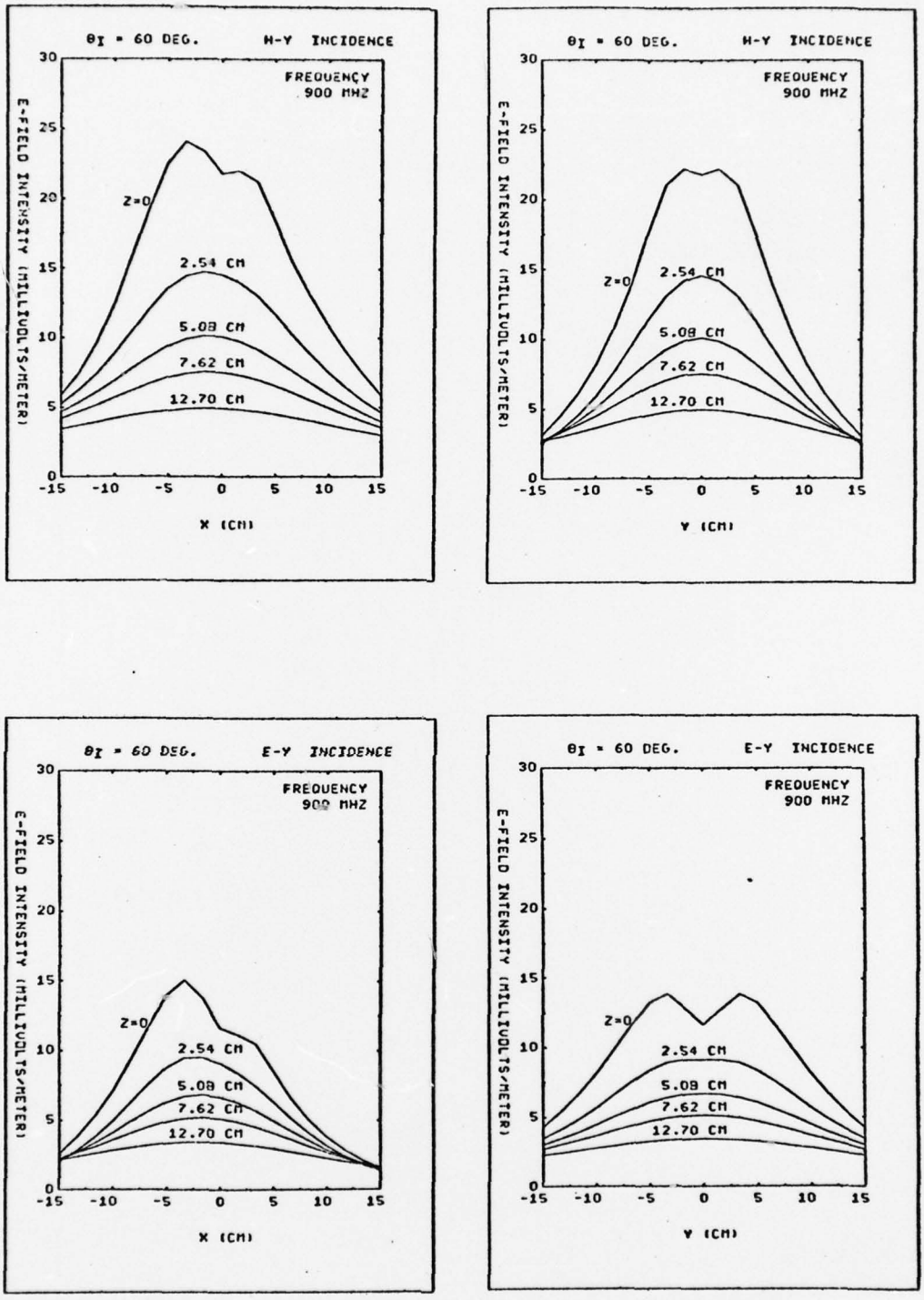

Figure 31. Parametric curves of z for the scattered E-field for incident angle $\theta_i = 60°$ at frequency = 900 MHz

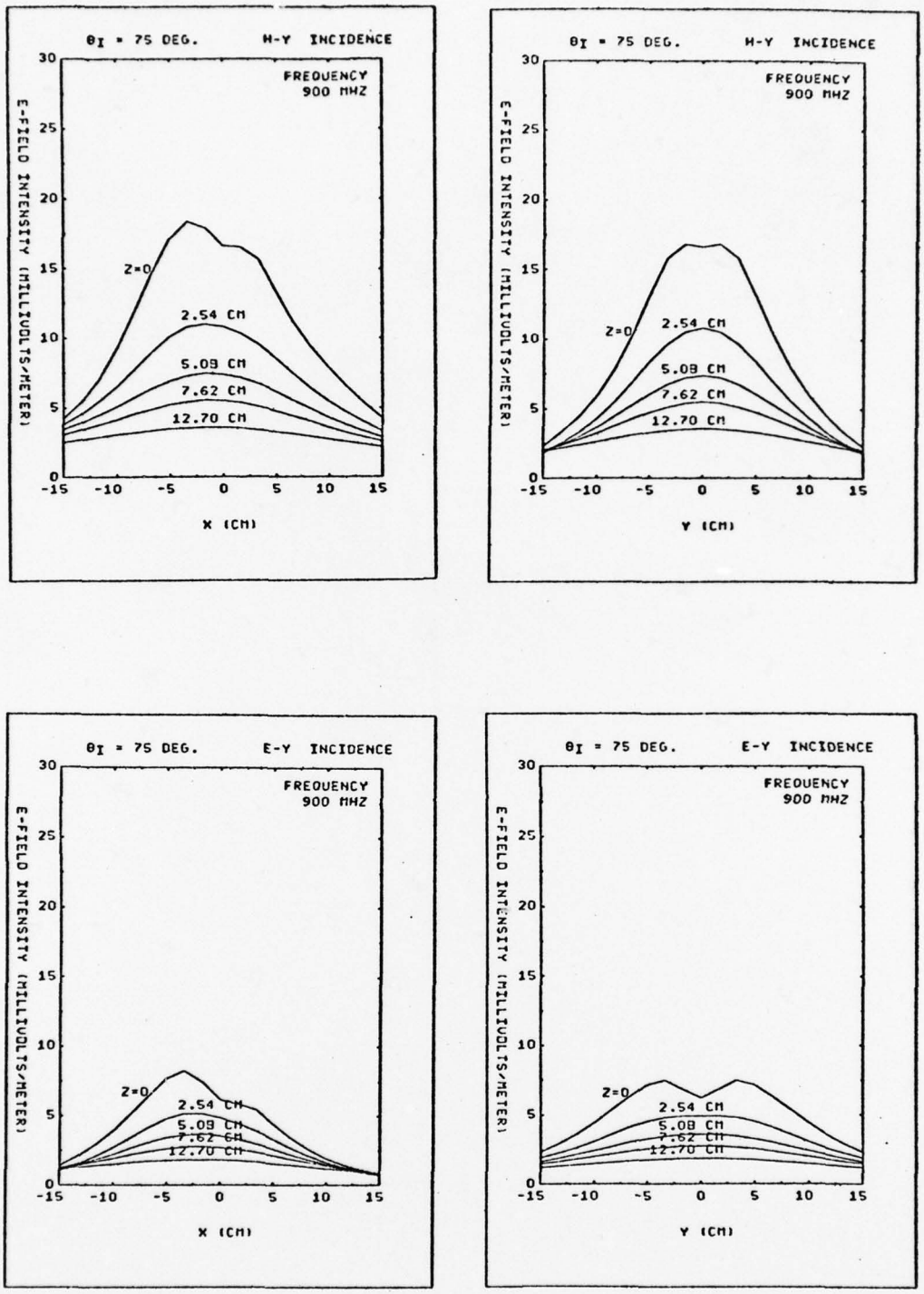

Figure 32. Parametric curves of z for the scattered E-field for incident angle θ_i = 75° at frequency = 900 MHz

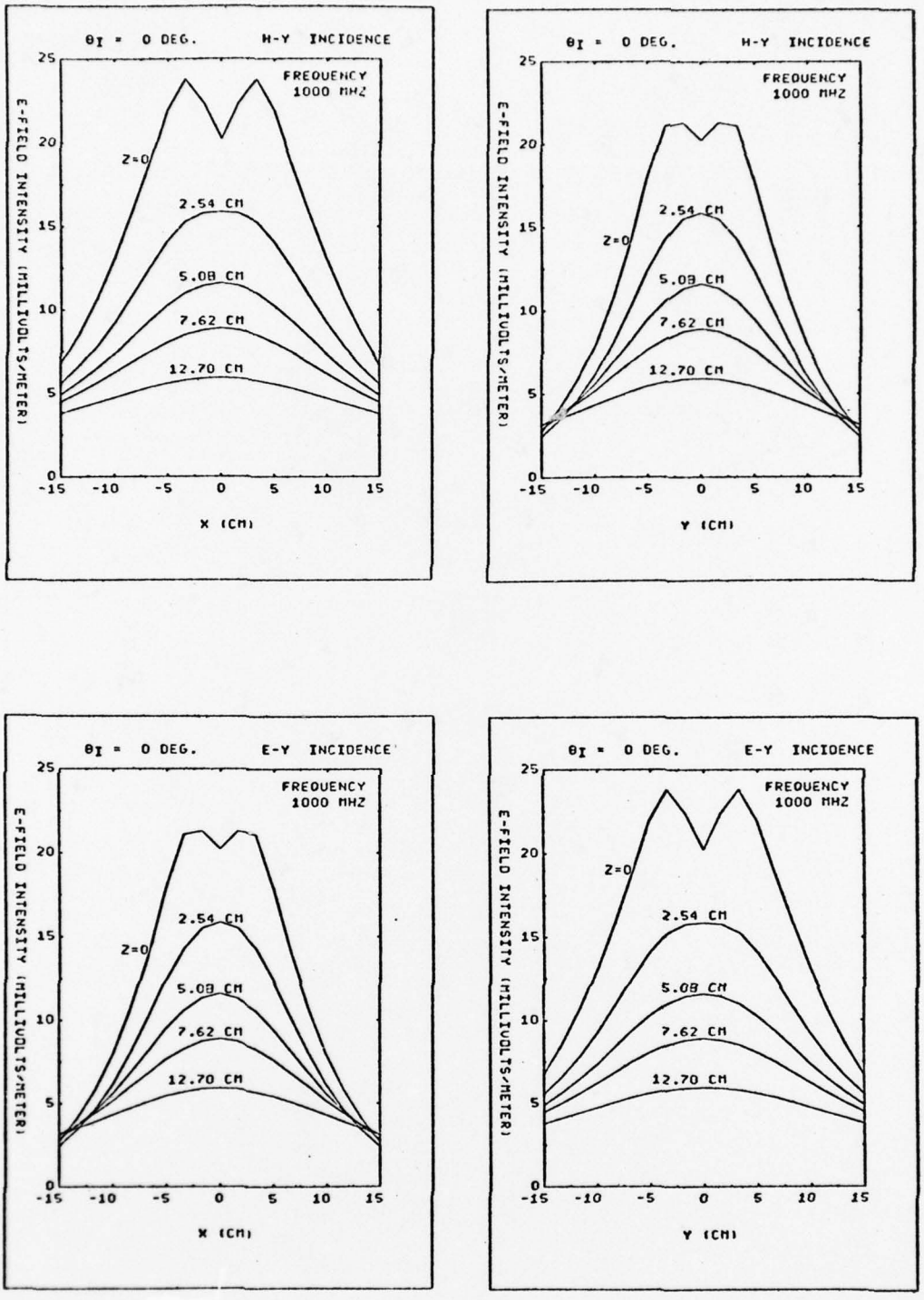

Figure 33. Parametric curves of z for the scattered E-field for incident angle $\theta_i = 0°$ at frequency = 1000 MHz

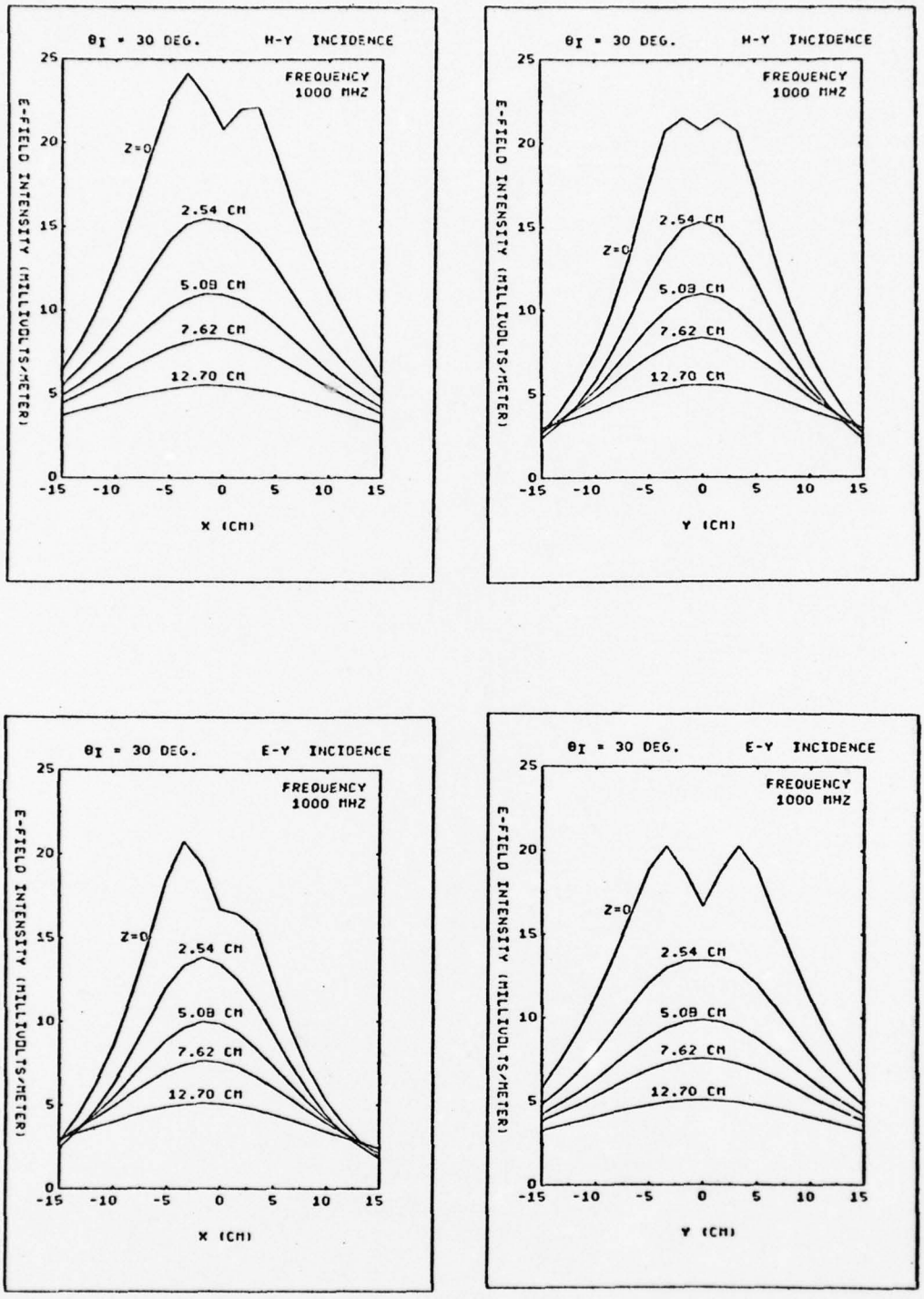

Figure 34. Parametric curves of z for the scattered E-field for incident angle θ_i = 30° at frequency = 1000 MHz

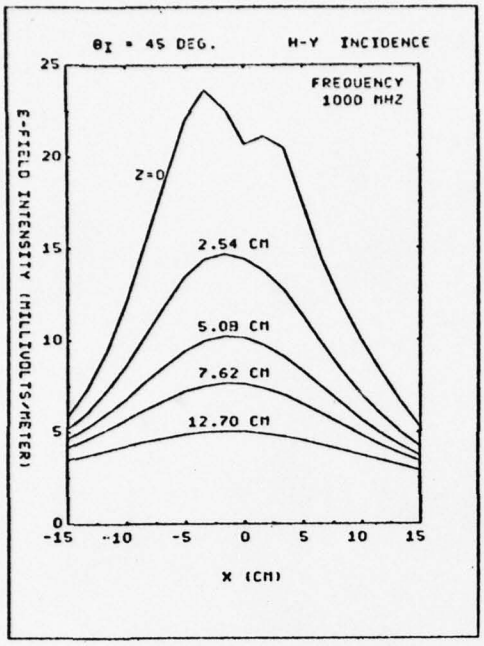

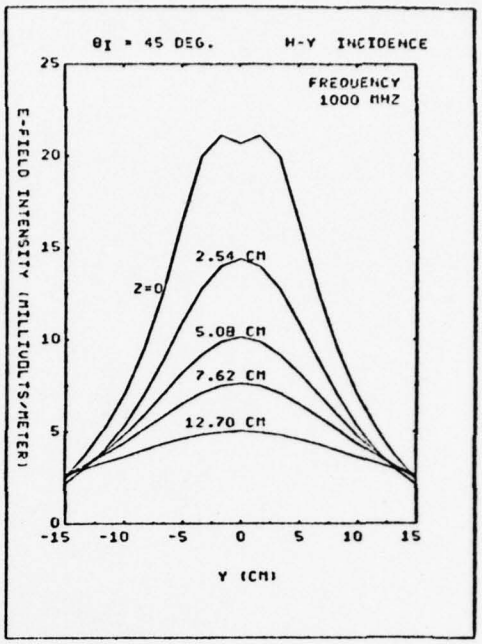

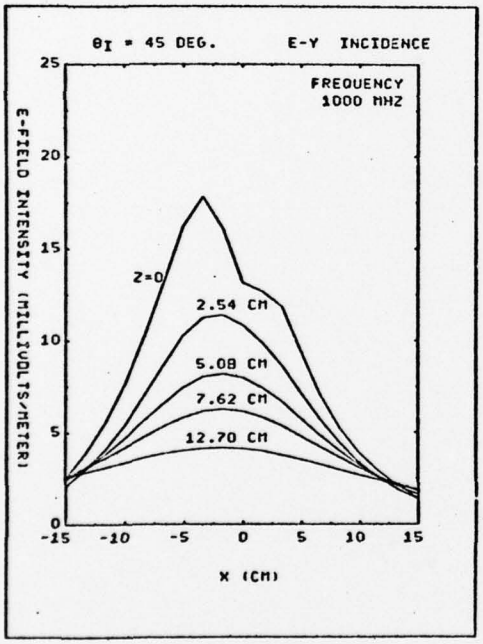

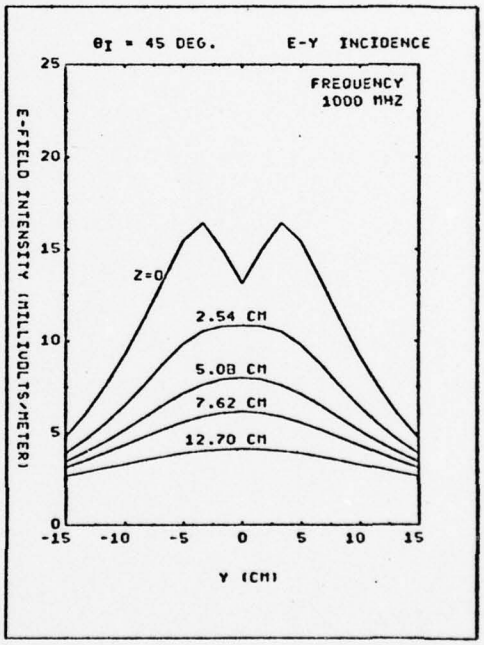

Figure 35. Parametric curves of z for the scattered E-field for incident angle θ_i = 45° at frequency = 1000 MHz

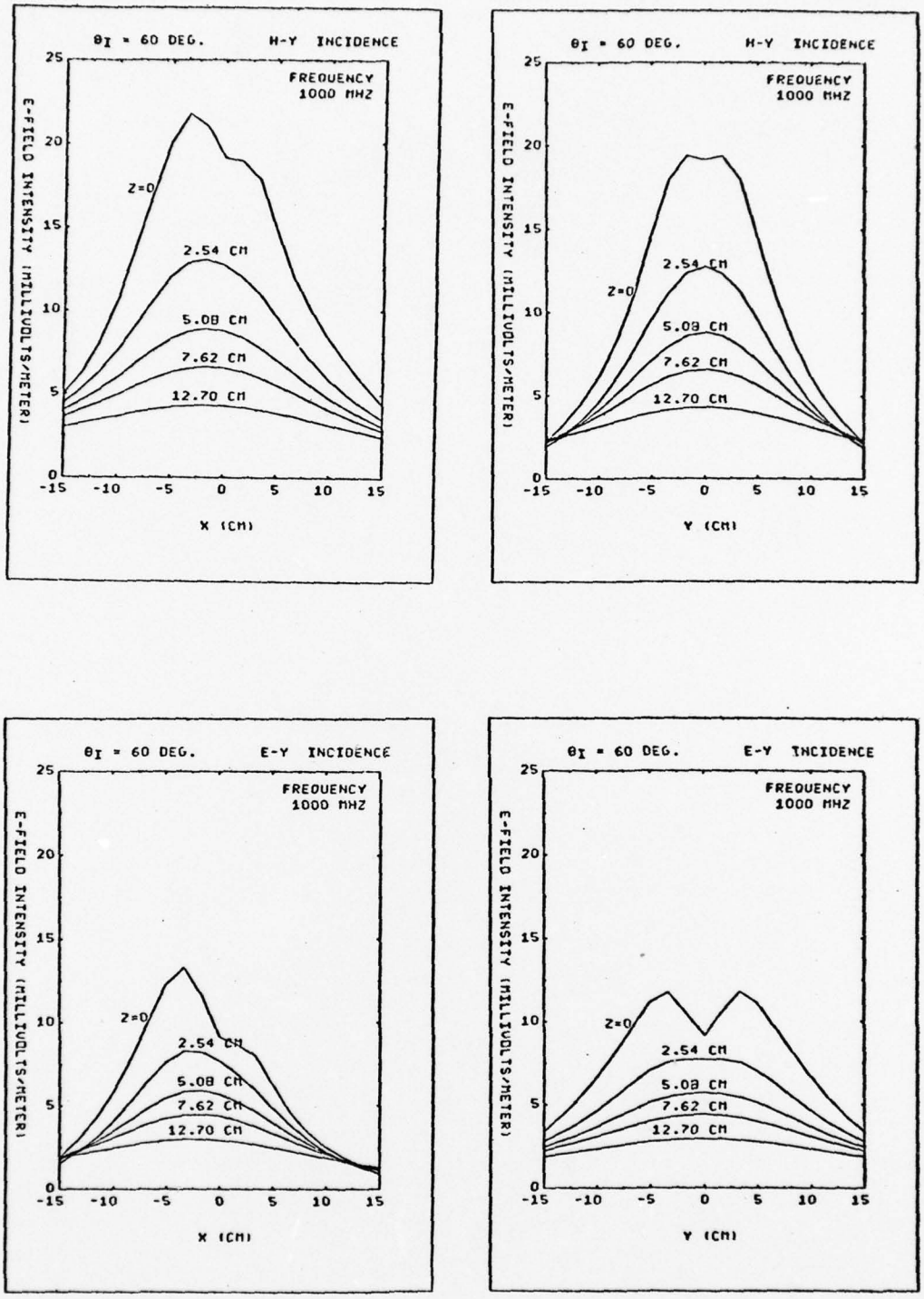

Figure 36. Parametric curves of z for the scattered E-field for incident angle $\theta_i = 60°$ at frequency = 1000 MHz

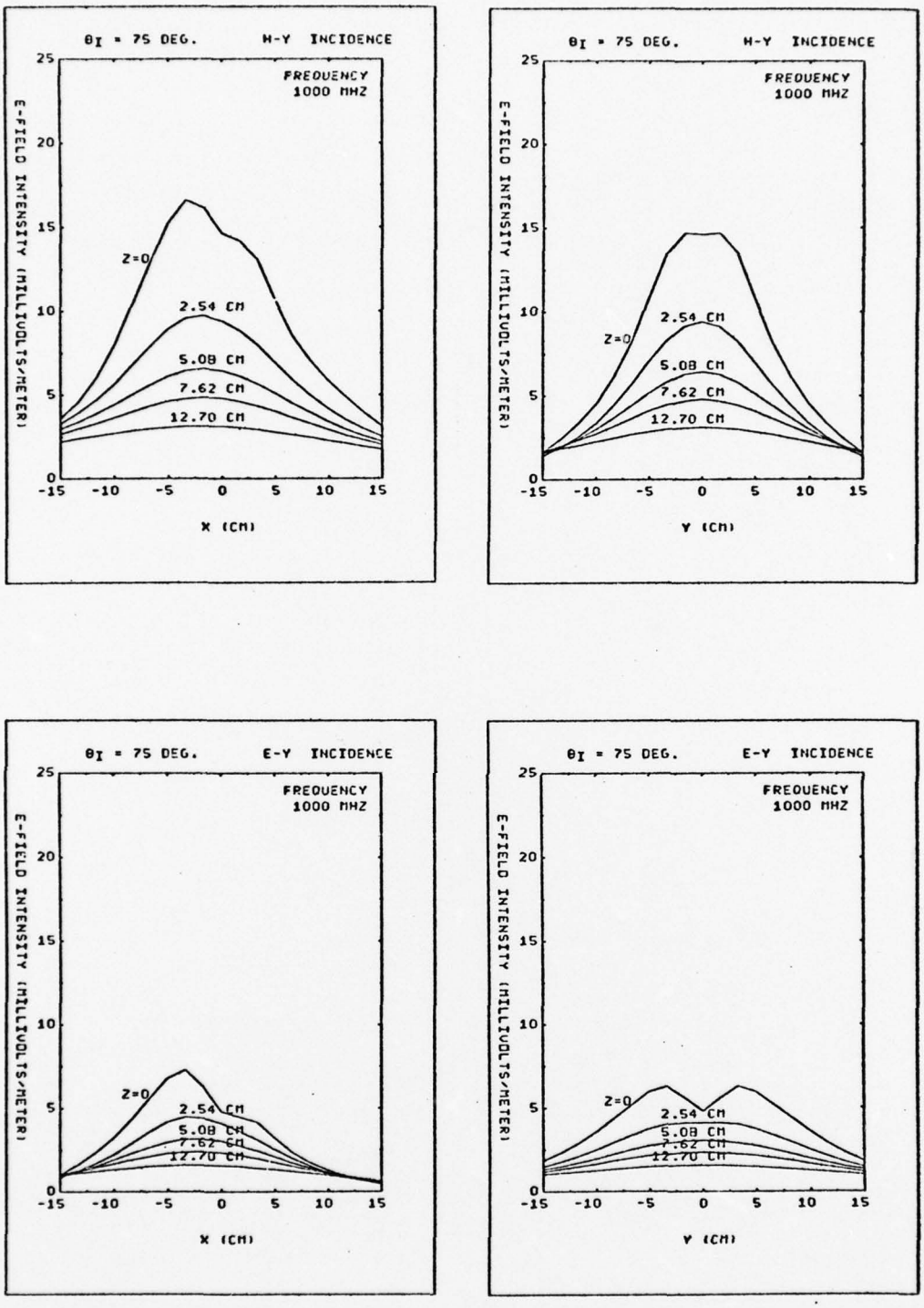

Figure 37. Parametric curves of z for the scattered E-field for incident angle θ_i = 75° at frequency = 1000 MHz

IV. CONCLUSIONS AND RECOMMENDATIONS

This investigation has applied the unimoment method to compute the scattering of electromagnetic waves by buried dielectric land mines. The unimoment method uses a sophisticated expansion technique to terminate the finite element method (FEM) computations at a mathematical sphere which encloses the land mine. The computation efficiency is greatly increased because the FEM calculations can be minimized by selecting the proper spheres.

The scattering fields obtained in this report include those of various incident angles and incident polarizations at several frequencies. The resulting E-fields are obtained on planes parallel to the ground surface. All these data will provide the engineers very clearly the effects of a buried dielectric land mine on the electromagnetic waves.

The results were presented in four different categories, i.e., (1) the 3-D and contour plots; (2) θ_i parametric studies; (3) frequency parametric studies; and (4) z parametric studies. The 3-D and contour plots show the complete pictures of the scattered field on the ground surface. The parametric studies provided comparisons of different parameters.

By examining the computational results in Section III, some findings of the scattered electric fields are summarized in the following:

(1) The peak values for $\theta_i = 0°$ on the ground are between 20 mV/Meter and 40 mV/Meter relative to 1 V/Meter incidence

(2) At frequencies higher than 700 MHz, the peak values occur at about $3 \sim 4$ cm from the center, while the center point above the mine is a local minimum.

(3) The dip of E-field at the center point disappeared at $z = 2.54$ cm or higher.

(4) At oblige incidences, the results of H-Y polarization are larger than those of E-Y polarization.

(5) The scattering amplitude increases as the frequency decreases.

(6) The amplitude decreases when the altitude is increased. For comparison, the peak values at $z = 12.70$ cm dropped to about $10 \sim 25\%$ of those on the ground.

With the capability of unimoment method in generating the scattering results by buried land mines, we would like to recommend the following studies as a natural extension to this investigation:

(1) Some of the antipersonnel land mines have a metallic ring to clip on the rubber. It is important to study the effects of the ring on the overall scattering effects.

(2) Only the uniform plane wave incidences were considered in this report. In the actual measurements, the antenna pattern has to be considered in the computations.

(3) We have used the earth dielectric constants $\varepsilon_e = 9 - j7$ for computations in this report. It will be of interest to study the effects due to the earth dielectric constants.

(4) Study the scattering by other objects such as rocks in order to be able to screen out their effects on the measurements.

REFERENCES

1. K.K. Mei, "Unimoment Method of Solving Antenna and Scattering Problems," IEEE Transactions on Antennas and Propagation, AP-22, pp. 760-766, November 1974.

2. R.E. Stovall and K.K. Mei, "Application of a Unimoment Technique to a Biconical Antenna with Inhomogeneous Dielectric Loading," IEEE Trans. on Antennas and Propagation, Vol. AP-23, No. 3, 335-342, May 1975.

3. S.K. Chang and K.K. Mei, "Application of the Unimoment Method to Electromagnetic Scattering of Dielectric Cylinders," IEEE Trans. on Antennas and Propagation, AP-24, No. 1, 35-42, January 1976.

4. M.A. Morgan and K.K. Mei "Finite-Element Computation of Scattering by Inhomogeneous Penetrable Bodies of Revolution," URSI International Electromagnetic Symposium, Palo Alto, CA, June 1977.

5. K.K. Mei, M.A. Morgan, and S.K. Chang, "Finite Methods in Electromagnetic Scattering," Chapter 10 in Electromagnetic Scattering, edited by P.L.E. Uslenghi, Academic Press, 1978.

6. S.K. Chang and K.K. Mei, "Generalization of Sommerfeld Integrals and Field Expansions in Two-Medium Half Spaces," Submitted to IEEE Trans. on Antennas and Propagation for publication in 1979.

7. S.K. Chang, "On Electromagnetic Wave Scattering by Buried Obstacles," Ph.D. Dissertation, June 1977.